# The Teton–Yellowstone Tornado of 21 July 1987

T. THEODORE FUJITA

Reprinted from MONTHLY WEATHER REVIEW, Vol. 117, No. 9, September 1989
American Meteorological Society

# The Teton–Yellowstone Tornado of 21 July 1987

T. THEODORE FUJITA

*The University of Chicago, Chicago, Illinois*

(Manuscript received 29 August 1988, in final form 24 March 1989)

ABSTRACT

The Teton–Yellowstone Tornado, rated F4, crossed the Continental Divide at 3070 m, leaving behind a damage swath 39.2-km long and 2.5-km wide. A detailed damage analysis by using stereo-pair and color photos revealed the existence of four spinup swirl marks and 72 microburst outflows inside the damage area. The tornado was spawned by a mesocyclone that formed at the intersection of a mesohigh boundary and a warm front. The parent cloud of the tornado, tracked on eight infrared-temperature maps from GOES East and West, moved at 25 m $s^{-1}$ and the number of cold temperature pixels below −60°C reached a distinct peak during the tornado time. Identified and tracked also are two warm spots enclosed inside the cold anvil cloud. On the basis of their identity and movement, an attempt was made to explain the cause of these spots as being the stratospheric cirrus clouds.

## 1. Introduction

Tornadoes in Wyoming are infrequent. Flora (1954) describes that only 61 tornadoes were reported in the 37.5 years ending with June 1953. This frequency is attributed to the low population density and public awareness in early years. The distribution of tornadoes between 1930 and 1978 in Fig. 1 reveals that most Wyoming tornadoes occurred on the east side of the Continental Divide, with lesser frequencies toward the Divide. From this statistical point of view, the 21 July tornado occurred at a most unlikely place, where a tornado of this intensity would not be expected to occur.

As shown in Fig. 2, a large number of tornadoes in 1987 occurred in a horseshoe-shaped area, connecting the states: Florida, Mississippi, Texas (Panhandle), Colorado, Minnesota, Michigan, and New Jersey. No tornado was reported from Tennessee, located near the center of the horseshoe, whereas 11 tornadoes occurred in Wyoming in 1987. It should also be noted that Edmonton, Canada was hit by a rare F4 tornado on 31 July 1987 that killed 26 persons and injured over 300 others.

Although a number of tornadoes have been reported from the Rockies at high elevations, most damage paths are rather short and narrow in comparison with their Midwestern counterparts. An early report of a massive blowdown on 21 July 1987 in the Teton Wilderness by the U.S. Forest Service indicated that one million trees in a 61-$km^2$ (15 000-acre) area were uprooted. In order to document the rare damage for identifying the nature of the storm, the author arranged the following three survey missions:

*30 July–2 August 1987.* An initial survey by James W. Partacz on board a Cessna aircraft, obtaining 430 color pictures.

*19 August 1987.* Contracted American Reprographics Inc., to take 28 vertical, stereo-pair pictures on 23 × 23 cm negatives. These pictures cover the entire area of the damage across the Continental Divide.

*27–31 August 1987.* After an inspection of these stereo-pictures, a detailed aerial photography from a low-flying Cessna was made by Brian E. Smith (940 photos) and the southernmost area was visited on foot by Bradley S. Churchill (90 photos).

An overall damage swath mapped from these aerial photos revealed that the path was 39-km long with a 3.9-km maximum width (see Fig. 3). A close examination of aerial photos also revealed the existence of cyclonic winds evidenced by the direction of uprooted trees. Was this storm a large tornado? The answer is "yes" because the National Weather Service and the precedent U.S. Weather Bureau have been classifying thunderstorm-induced damaging winds into (A) straight-line wind when damage directions are straight and (B) tornado when a funnel cloud was witnessed or rotational winds were evidenced by damage analyses. Tornadoes in the United States have long been confirmed on the basis of this classification, which cannot be altered without upsetting the long-term statistics.

*Corresponding author address:* Prof. T. Theodore Fujita, Department of Geophysical Sciences, The University of Chicago, 5734 Ellis Avenue, Chicago, IL 60637.

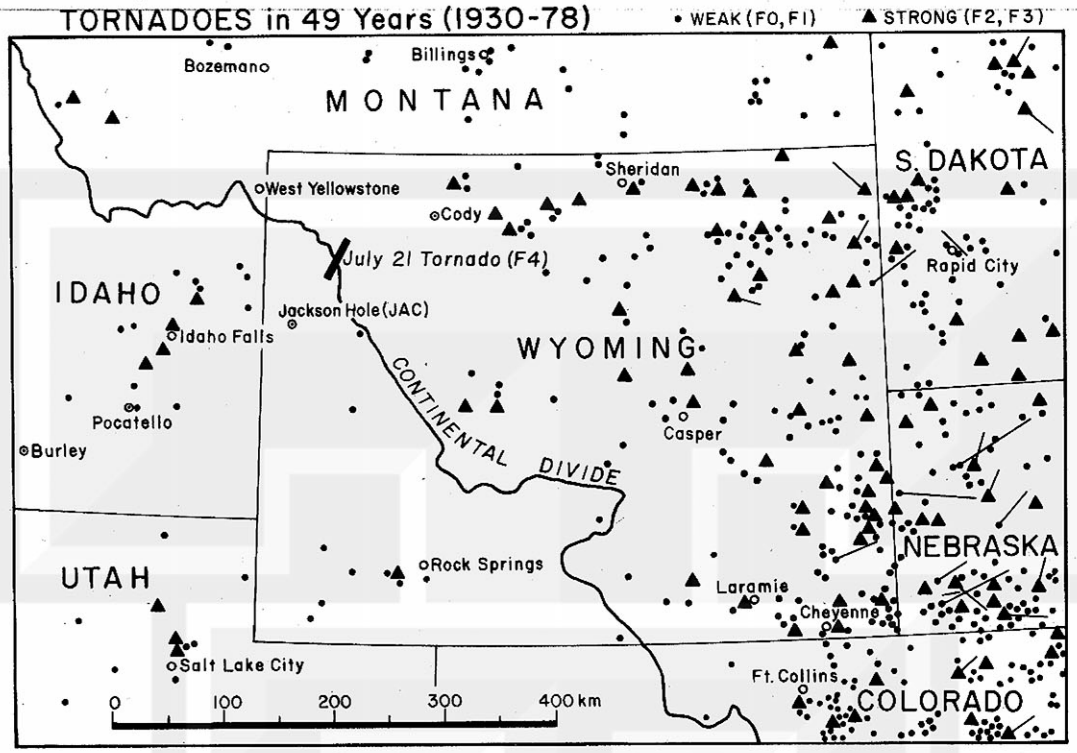


FIG. 1. Distribution of 194 tornadoes in Wyoming during the 49-year period, 1930–78. Average numbers are approximately four per year. From U.S. Tornado Map for National Weather Service Offices.

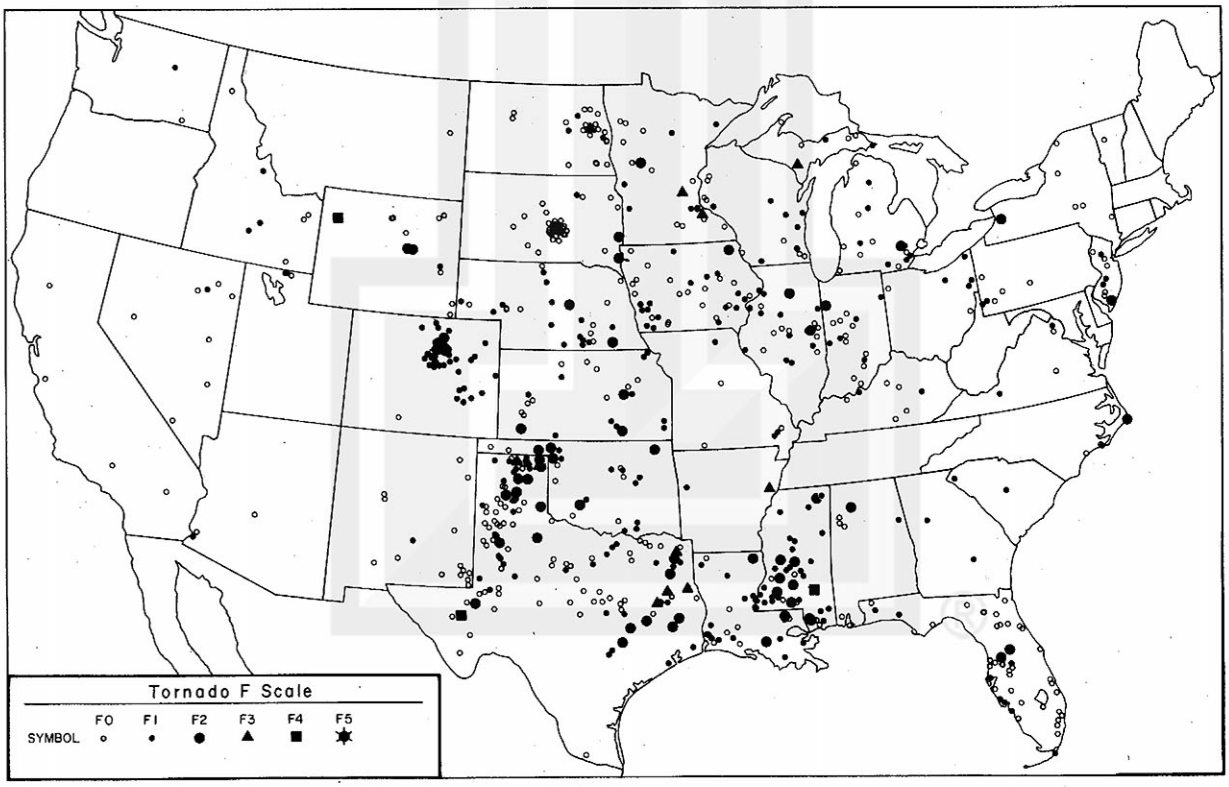


FIG. 2. Distribution of 657 tornadoes confirmed during 1987. This map was produced through multiple exposures of 12 monthly tornado maps in STORM DATA (1987).

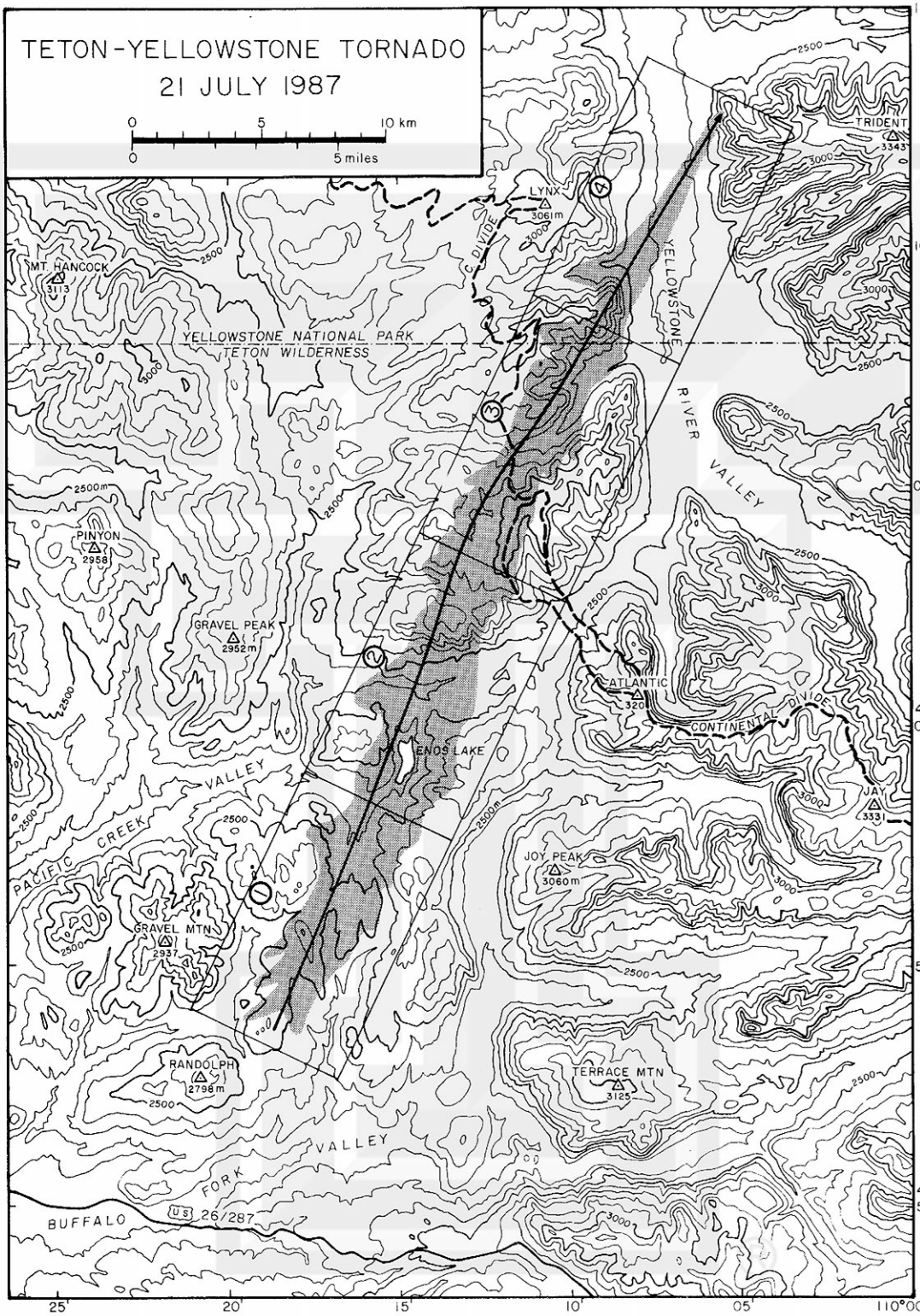


FIG. 3. An overall damage area of the Teton–Yellowstone Tornado which crossed the Continental Divide at 3070 m (10 070′). Detailed damage patterns inside the 39-km long and 2.5-km wide path are presented in four local maps 1, 2, 3, and 4.

TABLE 1. Comparison of Teton–Yellowstone tornado with 12 tornadoes in Carolinas spawned by a single mesocyclone of 28 March 1984. $W_{max}$ and $\bar{W}$ denote the maximum and mean damage widths determined by the National Weather Service and the University of Chicago. Refer to STORM DATA (1984).

| Tornado identification | Touchdown (local time) | $W_{max}$ | $\bar{W}$ | Length (km) | Deaths | Injuries |
|---|---|---|---|---|---|---|
| Teton–Yellowstone T., WY | 1328 MST | 3.9 km | 2.5 km | 39 | 0 | 0 |
| Newberry Tornado, SC | 1720 EST | 1.3 | 0.9 | 37 | 1 | 38 |
| New Hope Tornado, SC | 1740 | 1.2 | 0.8 | 31 | 0 | 10 |
| Winnsboro Tornado, SC | 1800 | 1.4 | 0.9 | 55 | 5 | 49 |
| Kershaw Tornado, SC | 1820 | 0.5 | 0.5 | 6 | 0 | 36 |
| Sandhill Tornado, SC | 1840 | 0.5 | 0.5 | 2 | 0 | 0 |
| Cash Tornado, SC | 1845 | 1.4 | 0.6 | 11 | 0 | 24 |
| Bennettsville Tornado SC–NC | 1910 | 4.0 | 1.9 | 37 | 7 | 100 |
| McColl Tornado, SC–NC | 1920 | 3.9 | 2.4 | 72 | 5 | 395 |
| Big Swamp Tornado, NC | 1945 | 2.4 | 1.3 | 66 | 12 | 106 |
| Mount Oliver Tornado, NC | 2015 | 1.6 | 1.3 | 34 | 3 | 149 |
| La Grange Tornado, NC | 2030 | 1.1 | 0.5 | 14 | 0 | 81 |
| Ayden Tornado, NC | 2045 | 1.9 | 1.1 | 61 | 16 | 153 |

Although such a large tornado is rare, 1.6 km (1 mile) or wider damage swaths have been reported from various parts of the United States. A notable example of a family of wide-path (1.6 km or wider) tornadoes of 28 March 1984 is presented in Table 1. Of these 12 tornadoes spawned by a single mesocyclone which traveled 445 km from South Carolina to North Carolina, five were wide-path tornadoes. Damage swaths of wide-path tornadoes are classified into narrow start and wide start and the shape of their damage areas vary with the traveling motion of tornadoes (see Fig. 4). The well-known Tri-state tornado of 18 March 1925 reported by Root and Barron (1925) was a narrow-start (200-m wide), fast-moving tornado and the Grand Island tornado reported by Fujita (1981) was a wide-start (2.5-km wide), slow-moving tornado. This Teton–Yellowstone tornado was a wide-start, fast-moving tornado.

The foregoing definition of tornado appears to be simple and straightforward. However, the confirmation procedure of tornadoes is rather complicated, because a tornado is often characterized by smaller-scale embedded vortices and surrounded by a larger-scale rotational airflow. One type of the smaller-scale vortices are suction vortices proposed by Fujita (1971) and confirmed by Agee et al. (1975) and many others. While these suction vortices orbit around the core of strong tornadoes, the spinup vortex near the center of a large tornado swirls only momentarily and disappears, leaving behind a swirl pattern of uprooted trees.

The "tornado cyclone," a larger-scale cyclone in which one or more tornadoes are embedded, was identified by Brooks (1949). Since then, Fujita et al. (1956) called the cyclone "mesocyclone," because the cyclone could persist before and after the tornado-bearing stage. Brown et al. (1971) detected by single Doppler radar the airflow of a developing radar hook echo and Lemon et al. (1978) found the intensification of mesocyclone circulation aloft prior to the tornado-bearing stage. Intensification of Del City–Edmond and Harrah mesocyclones at low elevation prior to the tornado formation was revealed by Brandes (1981, 1984), emphasizing the importance of the mesocyclone circulation in predicting and warning of tornadoes.

On the other hand, these studies suggest a possibility that a mesocyclone could induce damaging winds over a large area prior to a tornado formation. In search of a possible mesocyclone damage, an 8-km wide and 20-km long area to the south of the touchdown location of the Teton–Yellowstone tornado was searched from the air. Both sides of the 15-km stretch of U.S. Highway 26 in Fig. 3 were also searched by car, finding no tree damage in the suspected area. Whereas the tornado damage, after touchdown, increased from F0 to F4

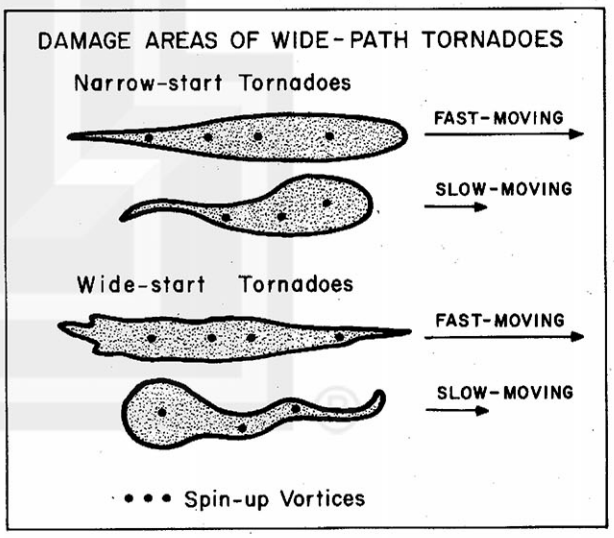


FIG. 4. Typical damage swaths of wide-path tornadoes. The Teton–Yellowstone storm was a wide-start, fast-moving tornado. Spinup vortex marks, 50 to 500 m in individual diameter, are swirls of uprooted trees located inside a wide-path swath.

within less than a 5-km distance or a 3-min travel time at 25 m $s^{-1}$. Based on these findings, it was concluded that the tornado intensified very quickly inside a parent mesocyclone which was not accompanied by a damage-causing wind on the ground.

## 2. Mapping of the damage

In addition to the standard United States Geological Survey (USGS) 1:250 000 maps, three types of topographic maps were used in mapping the direction of fallen trees. These maps are:

*1:24 000 USGS 7.5-Minute Maps (south of 44°N)*

Topography from 1964 aerial photographs, contour interval 40 ft, forest areas in green.

*1:62 500 USGS 15-Minute Maps (north of 44°N)*

Topography from 1954 aerial photographs, contour interval 80 ft, forest areas in green.

*1:126 720 Forest Service Map (Bridger–Teton National Forest)*

Compiled in 1984, contour interval 50 m, no forest area indicated.

Two major problems encountered in using these maps are the difference in both scales and in contour intervals. The overall damage in Fig. 3 was mapped directly on the Forest Service map, while four local maps in Figs. 4–7 were made by enlarging and matching photographically the 15-Min and 7.5-Min maps into a unique scale. They were then remapped with a contour interval of 20 m.

### *a. From touchdown to liftoff*

The first indication of F1 damage was spotted in a valley 3 km to the northeast of Randolph Mountain. Thereafter, the damage path widened and gradually became organized toward the 2700-m Gravel Ridge. There was a very large area of devastation to the northeast of the ridge. The devastation continued toward Enos Lake, a beautiful emerald-colored lake at 2382-m MSL. After passing directly over the lake, the storm descended into Pacific Creek Valley at 2380-m MSL.

Damage on steep slopes was visible between the valley floor and a 2900-m plateau for several kilometers until it crossed the Continental Divide. The highest elevation of tree damage was confirmed at 3070-m (10 070-ft) MSL on the Continental Divide.

Severe tree damage occurred inside three cirques, bowl-shaped depressions carved by a glacier. After descending from these cirques, the storm crossed the headwaters of Falcon Creek and the path went up and down a number of cliffs until descending to the floor of the Yellowstone River Valley. Storm winds weakened gradually while passing over the flat valley floor at 2400-m MSL. On the other side of the valley, damage became spotty until wind effects disappeared on the slope at 2520-m MSL.

The Teton–Yellowstone Tornado left behind a 39.2-km (24.4-mi) long path with an average width of 2.5 km (1.6 mi), devastating the protected forest of the Teton–Yellowstone Wilderness. The highest F-scale damage confirmed inside the tornado area was F4, an intensity rarely experienced in the Rockies. Small spotty areas affected by F4 winds were characterized by flattened Engelmann spruce trees, 30 to 40 cm in diameter, spattered by wind-blown topsoil and debarked.

### *b. Four local damage maps*

The overall damage area in Fig. 3 was divided into four rectangular areas, Maps 1, 2, 3, and 4. Each area was enlarged and remapped with contour lines at 20-m intervals and forest areas were added for determining the location and the fall direction of damaged trees.

Map 1 (Fig. 5) covers the damage area from touchdown to the Enos Lake area. The most interesting damage patterns seen in this map are two spinup swirls A and B and 18 centers of diverging winds. These centers are located predominantly on top of small hills, but some are found in valleys. It is suspected that the diverging winds on the ground resulted from small downdrafts, 200 to 500 m in diameter, as they were intercepted by the high-elevation terrain extending into the storm cloud. In this paper, the author called these diverging winds at the roots of small downdrafts microbursts and they were numbered.

It will be seen later that the parent cloud of this tornado traveled at the rate of 25 m $s^{-1}$, from left to right across the local map. When intercepted by the ground, incloud downdrafts and diverging winds will move left to right on the map at a high translational speed. Because the tornado was rotating cyclonically as it moved across Map 1, the airflow, diverging out from each microburst center, was spiraling in toward the rotation center of the fast-moving tornado. Seen also in this local map are two swirl patterns, A and B, caused by two separate spinup vortices formed near the tornado center.

Map 2 (Fig. 6) includes the damage area from near Enos Lake to the plateau top, north of Pacific Creek. Centers of Microbursts 19 through 44 are seen in this map. Damage vectors show that some microburst centers are located on the upwind side of the steep slope, and the diverging winds blew violently upslope over cliffs in rugged terrain.

The tornado center crossed the left edge of this map at 9.7 path kilometers (the distance measured from the first damage) and departed at the right edge at 20.0 km, passing north of Enos Lake. At two locations, one in the Pacific Creek Valley and the other on the plateau, the cyclonic rotation of the tornado is clearly identifiable from the damage. Two curved outflows from

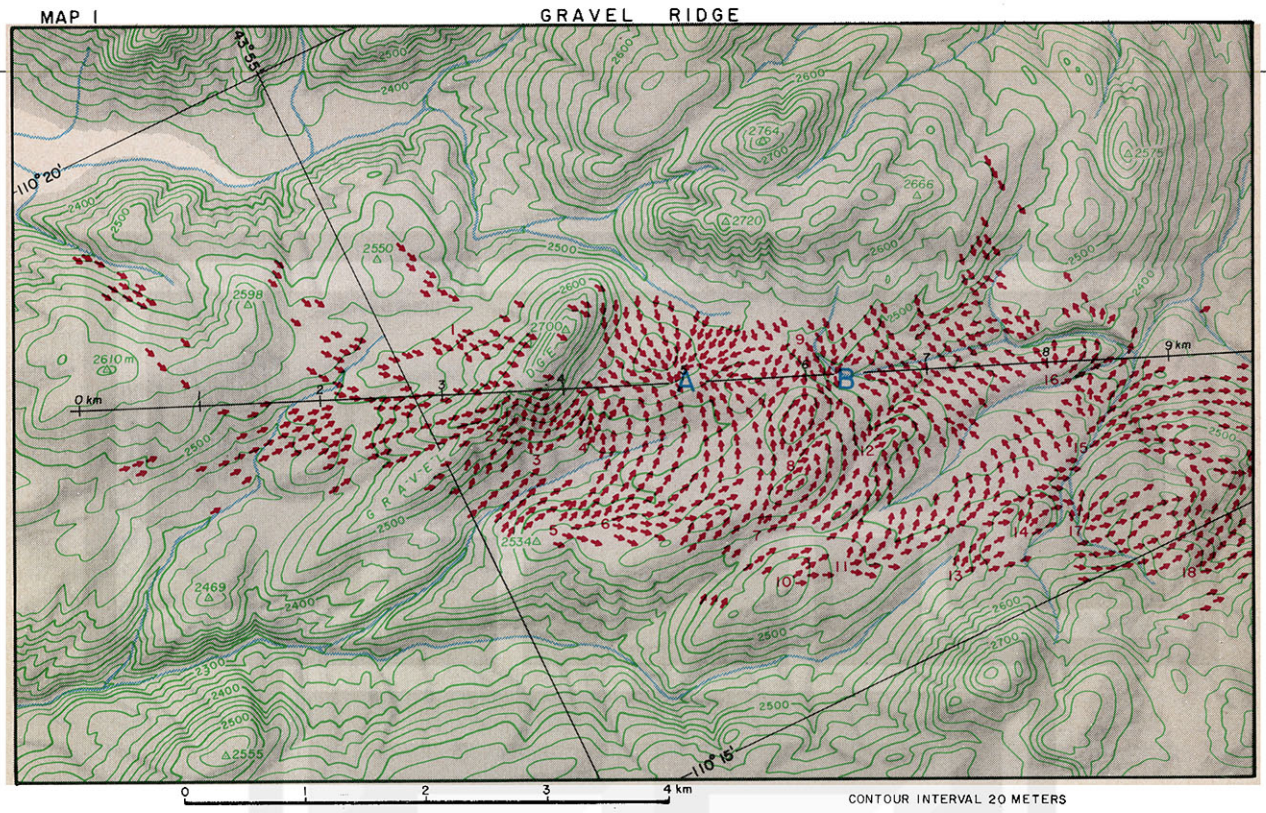


FIG. 5. Gravel Ridge section covering 0.0 to 9.7 path kilometers. Spinup Swirls A and B and 18 microbursts are in this map.

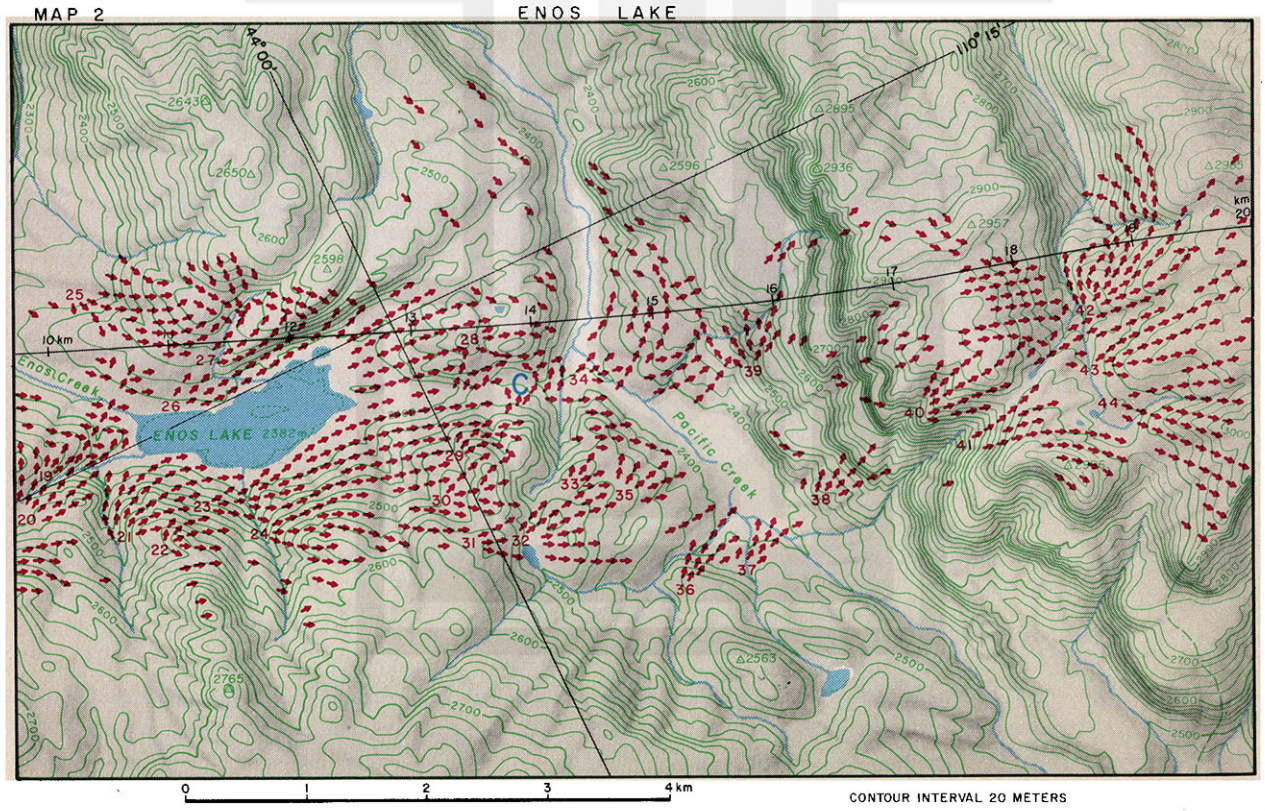


FIG. 6. Enos Lake section covering 9.7 to 20.0 path kilometers. Spinup Swirl C and 26 microbursts are in this map.

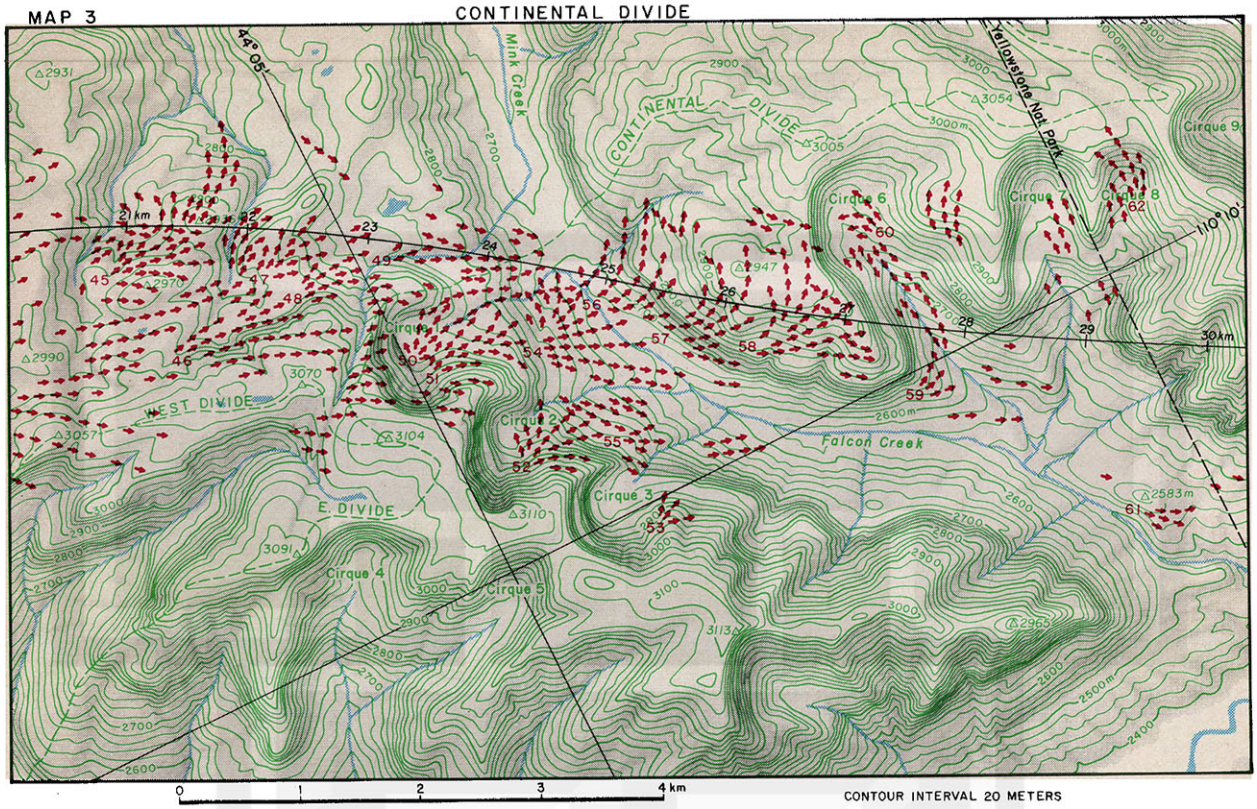


FIG. 7. Continental Divide section covering 20.0 to 30.3 path kilometers. Eighteen microbursts are in this map.

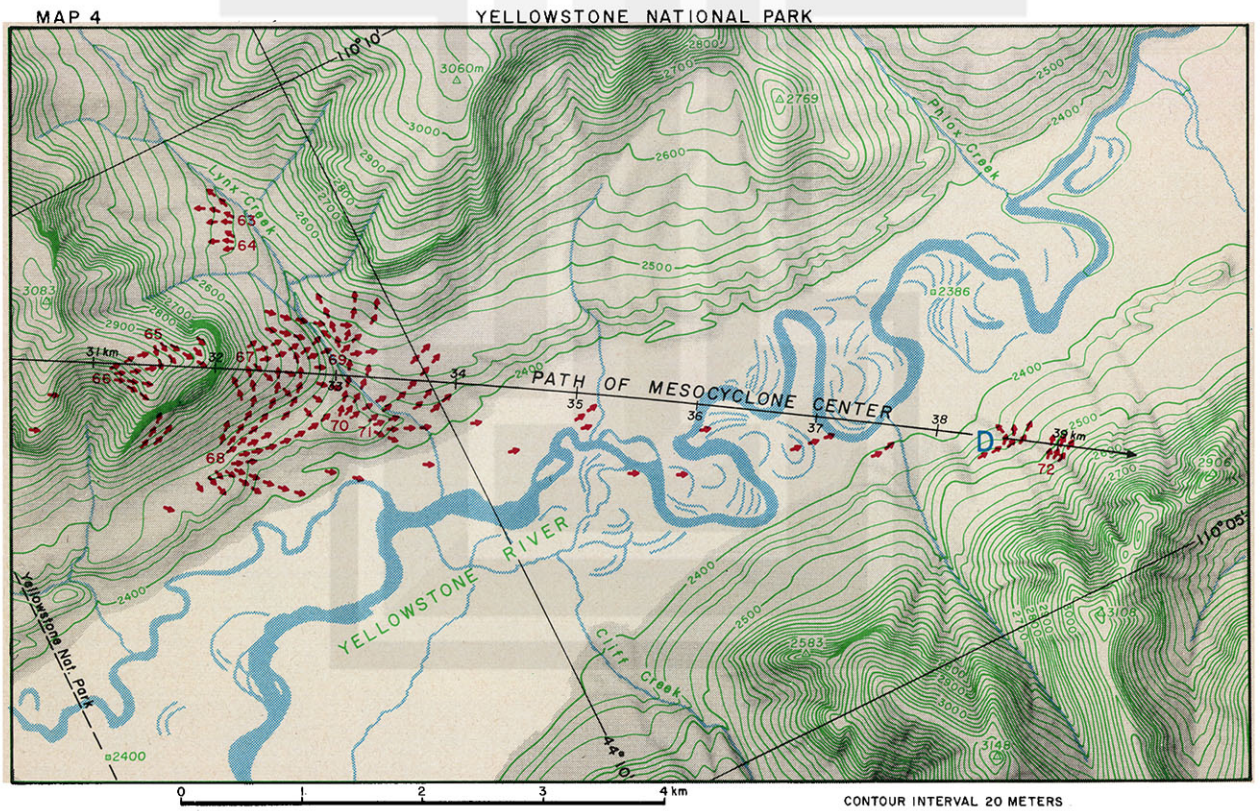


FIG. 8. Yellowstone National Park section covering 30.3 to 39.2 path kilometers. Spinup Swirl D and 10 microbursts are in this map.

FIG. 10. An F4 damage visible as a band of light brown color, extending left to right on small, low hills.
(Photo by James W. Partacz, looking west-northwest.)

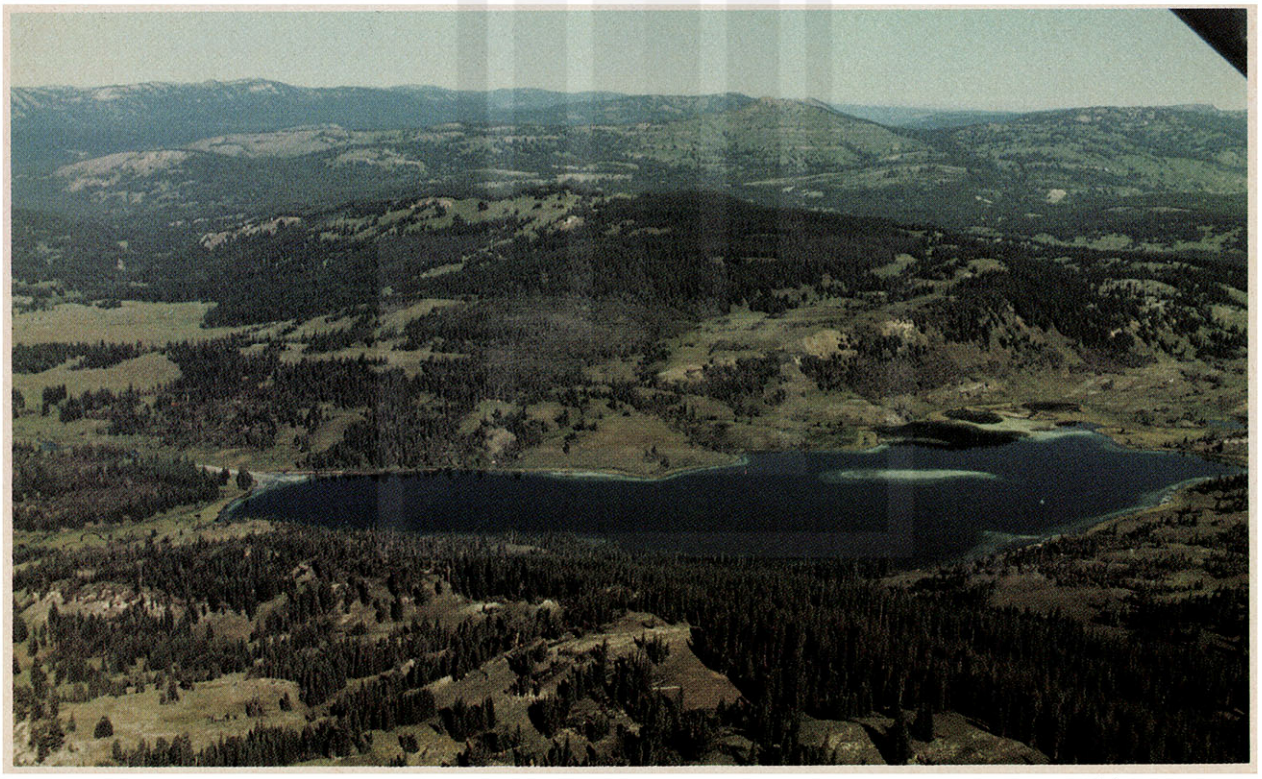

FIG. 11. A view of emerald-colored Enos Lake. Seen in the background are high peaks on the Continental Divide.
(Photo by James W. Partacz, looking west-northwest.)

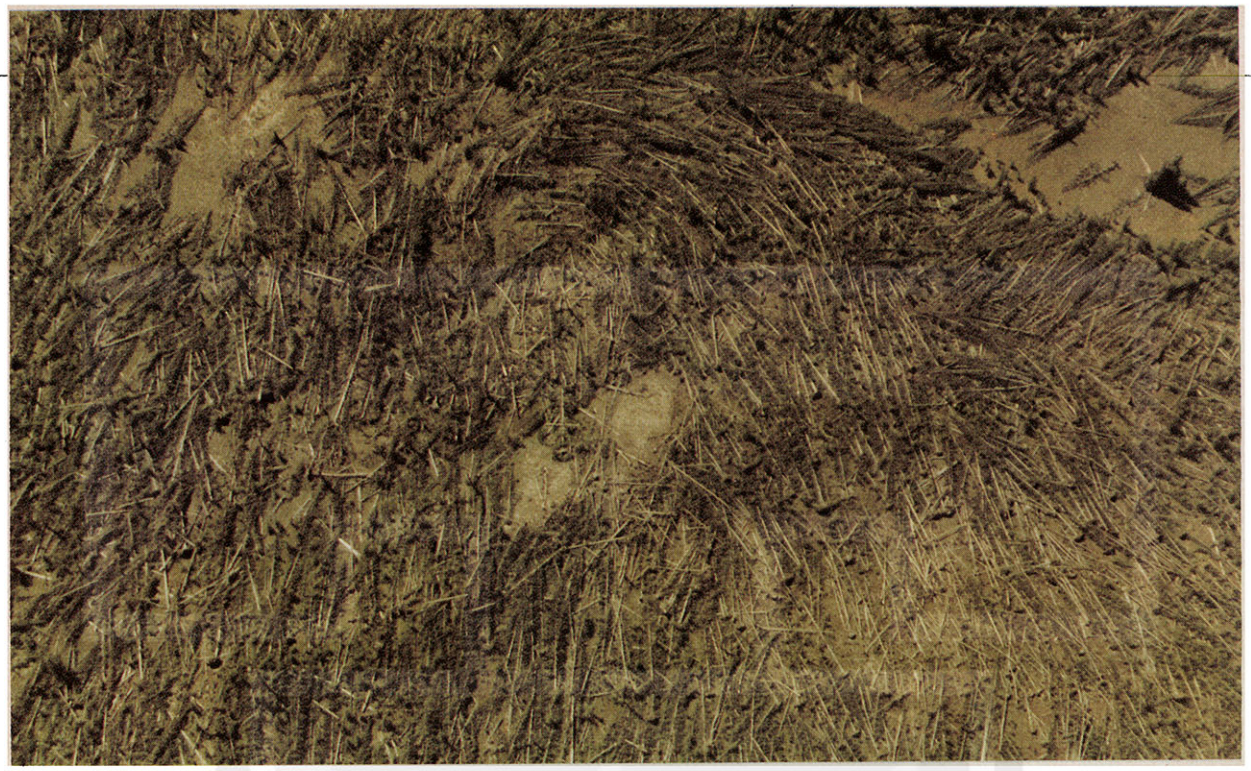

FIG. 12. A close-up view of spinup vortex mark A made visible by a swirling pattern of blown-down trees. (Photo by Brian E. Smith, looking west-southwest.)

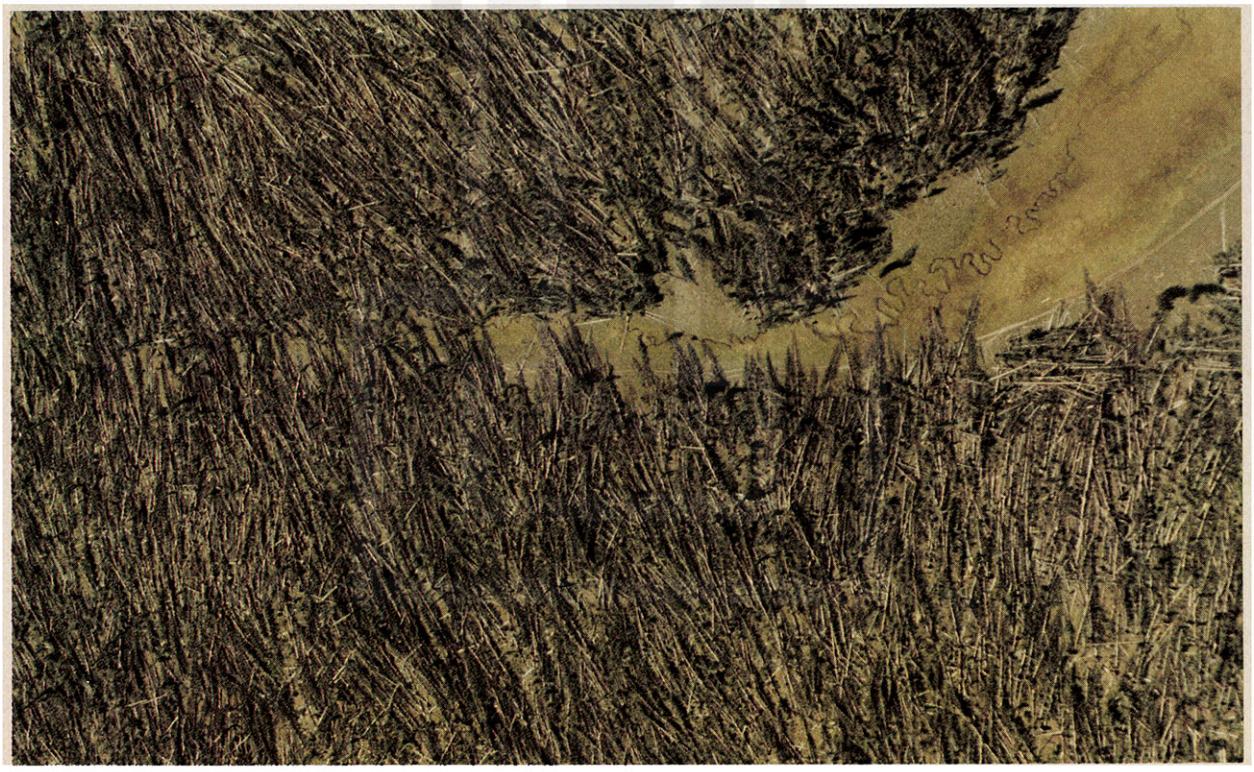

FIG. 13. A close-up view of blown-down trees inside Microburst 8. Fallen trees blocked Enos Lake Trail. (Photo by Brian E. Smith, looking west-southwest.)


FIG. 9. A portion of the vertical picture number 7, one of the 28 stereo pictures taken by a photographic aircraft on 19 August 1987, 29 days after the storm. An estimated 130 000 trees were blown down in the area of this picture.

Microbursts 34 and 42 suggest strongly that a large number of microbursts around the tornado center were the providers of the angular momentum required to maintain the tornado circulation against large orographic friction in boundary layers. Spinup swirl C was identified in a forest south of Pacific Creek. It was characterized by both swirling and random tree damage, implying that a spinup vortex was at a stationary position over the forest for a while.

Map 3 (Fig. 7) extends between path kilometers 20.0 and 30.3 of the tornado center. Curved outflows were evident from Microbursts 45, 54, 56, 57, 58, 59, 60, and 62. These microbursts account for nearly half of the 18 microbursts that descended in the area of this damage map. Of interest is the descent of four microbursts inside Cirques 1, 2, and 3. Each of these microbursts descended near the eastern side of each cirque. The similarity in the location of these in-cirque microbursts, relative to the cirque, suggests the geometry of the cirque played a significant role in inducing these microbursts.

Map 4 (Fig. 8) includes path kilometers between 30.3 and 39.2, the end of the path. Ten microbursts, 63 through 72, are shown in this local map. The area of the most active microbursts is seen to the south of the Yellowstone River. Two microbursts, 65 and 66, descended near the top of a 2950-m hill surrounded on three sides by sheer walls of rock. Microburst 67 landed at the foot of the sheer wall on the downwind side. Three more microbursts descended farther downwind toward the river.

Microburst activity across the river valley was insignificant, and no evidence of microbursts was found on the valley floor, in spite of the fact that numerous healthy trees were seen in the aerial photos. The final stage of the tornado wind was evidenced on the northside slope of the Yellowstone River Valley. Spinup vortex D was confirmed at 2450-m MSL and Microburst 72, the last of the microbursts, was found on the path of the tornado center at 2500-m MSL. The overall damage swath of the Teton–Yellowstone Tornado ended at the 39.2 path kilometer.

### c. *The F4 damage*

Damage patterns left behind by the Teton–Yellowstone Tornado are categorized into 1) spinup vortex up to 200 m in diameter, 2) microburst outflow, 1 to 3 km in major axis, and 3) tornado circulation, 2 to 3 km in radius of curvature. These three damage patterns are woven together by a succession of high winds into a huge carpet of fallen trees.

The vertical photograph in Fig. 9 covers 1.8 × 2.3-km area to the north of the 2700-m Gravel Ridge. Centers of five microbursts, numbers 4, 6, 7, 8, and 9 are identified in this picture, along with spinup vortex A located on the path of the tornado center, extending from left to right across the upper section of the photograph. This photo is a cut-out from a sequence of 28 vertical stereo photos taken on 19 August 1987.

A band of light brown color extends from left to right along the path of the tornado center. This band denotes the F4 damage (band of F4 winds) characterized by uprooted large trees, spattered by wind-blown topsoil and debarked. This band is visible in an oblique aerial photo in Fig. 10 taken from a distance of 2 km, looking west-northwest. It extends from left to right across the center of the picture on a gentle hillside.

The damage weakened toward Enos Lake drained by Enos Creek as seen in Fig. 11. The photo, looking west-northwest, shows the 2952-m Gravel Peak and 2958-m Pinyon Mountain in the background. Light-colored forests on the other side of Enos Lake are those damaged by Microbursts 22, 23, 24, 29, 30, and 31. The tornado center moved from left to right, on the slope of the background hills in this oblique aerial photograph.

A close-up of spinup vortex mark A is shown in Fig. 12. A distinct swirl is seen approximately 2 cm on the photo above two spots of bare ground; evidence of other indistinct swirls are also visible elsewhere in this picture. Fallen trees in the lower right were stripped of most leaves, and branches and trunks were debarked. The author has not seen such a devastating tree damage in the vicinity of structural F4 damage in cities such as Xenia, Ohio and Birmingham, Alabama, which he had investigated. The only F4 damage in a forest comparable to this one was photographed from a Cessna by the author in the Appalachians after the F4 Murphy Tornado in North Carolina on 3 April 1974.

Typical blowdown damage by a microburst is seen in Fig. 13, photographed half-way between the centers of Microburst 8 and spinup vortex A. The microburst center is located below the bottom of this photo and its outburst winds flattened tall trees, blocking the major Enos Lake Trail that extends across the photo into a meadow. It is amazing to count 2700 trees uprooted in the area of this photo covering only 0.08 $km^2$. The prorated number of trees blown down in the 4 $km^2$ area in Fig. 9 is 130 000. A total of one million trees were blown down by the storm.

### d. *Microbursts in cirques*

Three cirques near the Continental Divide are located on the east side of the path of the tornado center (see Figs. 7 and 14). The center of Cirque 1 is located 0.9 km away from the path, Cirque 2, 1.6 km, and Cirque 3, 1.9 km. A detailed analysis of damaging winds in and around these cirques revealed the existence of a microburst or a microburst family inside each cirque. Furthermore, positions of the microbursts relative to the cirque headwalls are almost identical. Such a distinct relationship between microbursts and topography was not seen in other parts of the damage area.

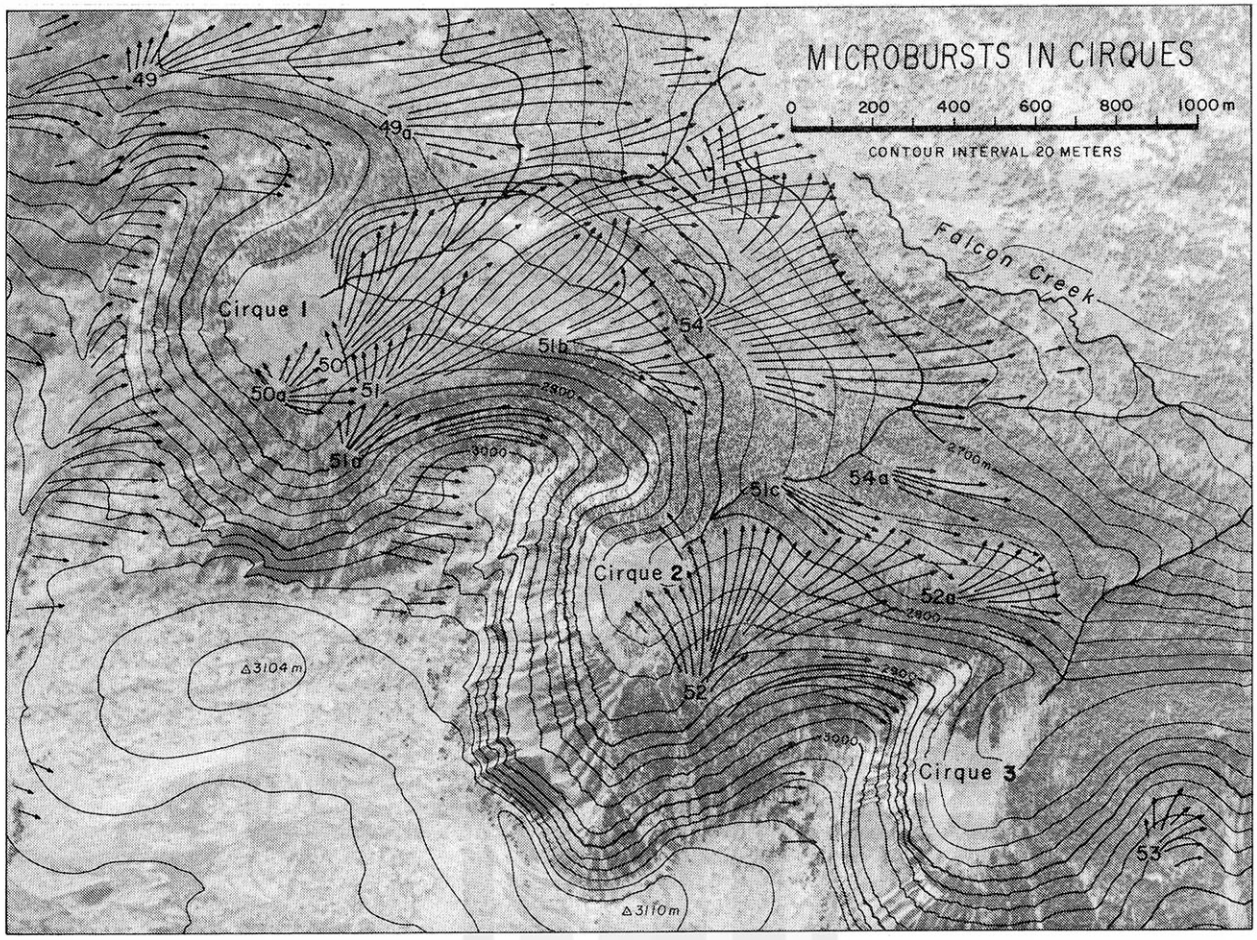


FIG. 14. Height contours (20-m interval) and damage directions superimposed upon the vertical aerial photo number 17 taken on 19 August 1987. Note that microbursts descended into three cirques.

Because the downflows inside the large tornado did not know where cirques were located beneath them, it is very unlikely that this microburst-cirque relationship was accidental. In an attempt to explain this relationship, it was hypothesized that the slanted downflow reaching the plateau of the preglacial surface slides down the surface of the headwall. The bowl-shaped surface will deflect the downflow into a focusing airflow which turns into a microburst upon reaching the ground inside the cirque (see Fig. 15). Table 2 was prepared to present geographic data applicable to these microbursts in three cirques. Note that the angle of descent of the focusing winds vary between 13° and 25°. Note also an increase in the F-scale microburst winds toward the path of the mesocyclone center.

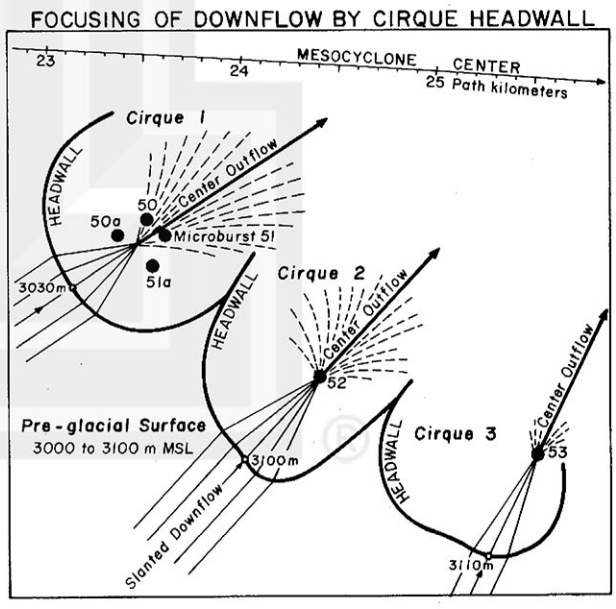


FIG. 15. A schematic figure showing the focusing of slanted downflows by cirque headwalls for inducing microbursts in cirques.

### *e. Angular momentum of large tornado over rugged terrain*

Let us first assume that a large tornado formed inside a mesocyclone passing over the Teton Wilderness area and began traveling over mountains. Thereafter, how

TABLE 2. Microburst winds in three cirques focused by arc-shaped headwalls. Microbursts are seen at the focal points inside cirques.

| | Cirque 1 | Cirque 2 | Cirque 3 |
|---|---|---|---|
| Height of headwall (m MSL) | 3030 | 3100 | 3100 |
| Height at microburst (m MSL) | 2860 | 2880 | 2980 |
| Height of descent (m) | 170 | 220 | 130 |
| Headwall to microburst (m) | 410 | 470 | 580 |
| Angle of descent (deg) | 23 | 25 | 13 |
| Microburst damage | F3 | F2 | F1 |

did the tornado maintain its fury against large frictional torques in the boundary layer over rugged terrain? The top diagram of Fig. 16 was prepared to show the ground elevation along the path of the tornado center and the middle diagram, the F-scale contours of the damage estimated from degradation of the tree damage. Apparently, the tornado intensified during the first 3 min while traveling from 0 to 5 path kilometers at 25 m $s^{-1}$. The peak intensity was maintained during the following 7 min, between 4 and 14 path kilometers. It then weakened significantly while passing over the 2900 to 3000-m plateau. This evidence confirms that the tornado worked hard in maintaining its circulation, suggesting the importance of the balance in the supply and loss of angular momentum.

The bottom diagram of Fig. 16 presents the center outflows of all microbursts in relation to the path of the tornado center. This diagram suggests convincingly that the angular momentum of the tornado was supplied by microbursts as their outburst winds spiraled into the tornado center. As expected, a strong microburst at a proper distance away from the tornado will generate the most effective torque in achieving an impulsive addition of angular momentum for intensifying the tornado.

In learning more about the impulsive addition of angular momentum, Fig. 17 was produced by relocating all of the 72 microbursts inside the damage area on coordinates relative to the tornado center. The position of each microburst was determined by shifting the microburst center along its path until the center outflow coincides best with the hypothetical spirals around the tornado center. This diagram reveals that a large number of the microbursts in the right-front quadrant contributed most, followed by those in the right-rear, left-front, and left-rear quadrants.

On the basis of the foregoing evidence, the author now classifies the evolution of the Teton–Yellowstone tornado into the following four stages:

1) Intensification Stage from 0 to 5 path kilometers—Strong microburst outflows on rolling hills in the right-front quadrant spiral in toward the tornado center

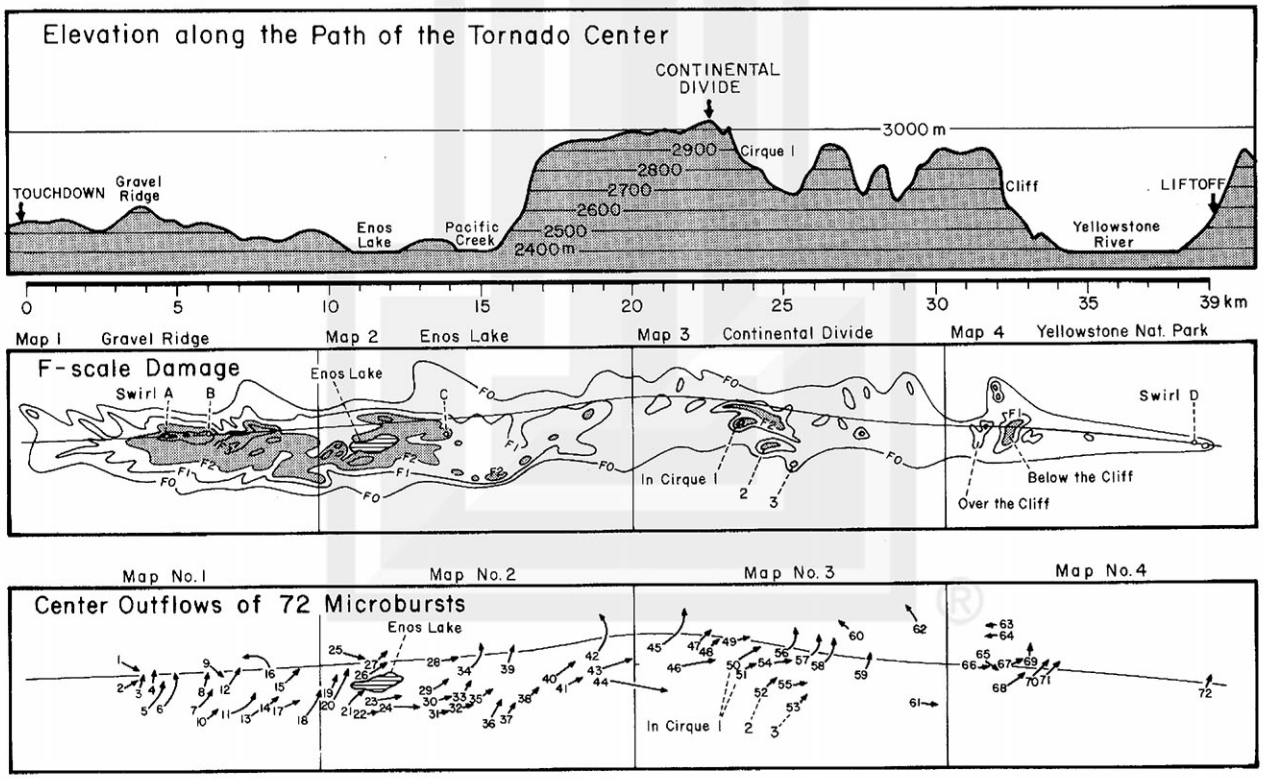


FIG. 16. Top: Elevation of the ground along the path of the tornado center. Middle: F-scale isotachs inside the damage area. Bottom: Center outflows of 72 microbursts, contributing to the impulsive addition of angular momentum.

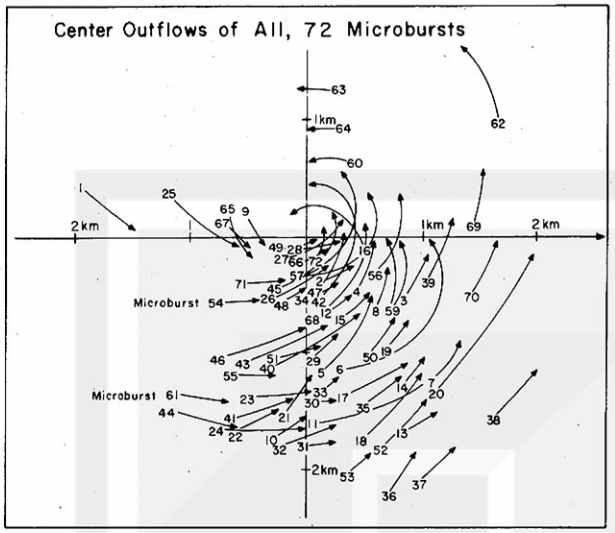


FIG. 17. Tornado-relative positions of 72 microbursts and their center outflows.

while the tornado damage increased rapidly from F0 to F4.

2) Mature Stage from 5 to 15 path kilometers—Tornado maintains the F2 to F3 intensity along with a wide damage width. Most microbursts are located in the right-front quadrant, 1 to 2 km from the tornado center.

3) Weakening Stage from 15 to 32 path kilometers—Tornado moves over the high plateau and rugged terrain near the Continental Divide. Location of microbursts becomes progressively closer to the tornado center line.

4) Dissipating Stage from 32 to 39 path kilometers—While traveling over the flat valley of the Yellowstone River, damage width narrows gradually to dissipation. Most microbursts are located near the tornado center.

## 3. Surface weather observations

An isolated wind damage was reported from Teton Village early in the afternoon of the tornado day. In confirming the nature of the damage, Smith and Churchill of the University of Chicago visited the site on 30 August 1987, finding 10 to 15 small trees pushed over in a field 7 km west-southwest of the Jackson Hole Airport (JAC). All trees were damaged by the straight-line wind from a 280° direction and no sign of a tornadic swirl was found. It is likely that the localized damage occurred approximately when JAC observed an 18 m $s^{-1}$ wind with a 26 m $s^{-1}$ (58 mph) gust from 280° at 1310 MST during a heavy thunderstorm with hail.

### *a. Was the tornado accompanied by a funnel cloud?*

Surface weather observations of this storm were made at the Jackson Hole Airport located 46 km (29 mi) southwest of the first damage. According to the observation log in Table 3, an overcast ceiling was at 2.4 km AGL (4.4 km MSL) and lasted from 1300 to 1550 MST. This MSL height is identical to that of the convective cloud base computed from the 00Z (1700 MST) sounding at Lander (LND), Wyoming. During the stormy weather at JAC between 1300 and 1345 MST, a lower ceiling at 900 m AGL (2900 m MSL) was observed. This height represents the low storm-cloud base, commonly seen beneath a cumulonimbus cloud. It is suspected that the base of the storm cloud in the tornado area was much lower than 2900 m MSL, the ceiling at JAC located 20 km to the west of the mesocyclone center at 1300 MST.

It is quite possible that the tornado cloud base was below the elevation of Enos Lake at 2382 m MSL, and the entire damage occurred just above the cloud base. Nine witnesses to the storm on a camping trip near Enos Lake told the U.S. Forest Service that they saw no funnel cloud and that the storm happened very quickly with a roar like a train in the distance. They noticed that golfball-sized hail pelted the ground. No other eyewitness has been found, so far, because one must walk or ride a horse for 5 km from the nearest road to the damage area.

### *b. Mesohigh and cold front*

Early in the morning of 21 July 1987 at 0500 MST (12Z), a cold front extended toward the southwest from the center of the 1001-mb cyclone over Hudson Bay, Canada. A small low-pressure area was located in northwestern Wyoming at the tail end of the cold front. Seen also on the surface map in Fig. 18 are thermal lows over the desert regions of Arizona, Nevada, and Oregon. There was a strong moisture inflow along the east side of these thermal lows where 13°C dewpoint temperatures were reported.

Thunderstorms began at Ely, Nevada at 0450 MST (1150 UTC) and at Salt Lake City, Utah at 0429 MST (1129 UTC), lasting 2 to 3 hours. The first sign of the mesoscale high pressure area (mesohigh) formed in southern Idaho and expanded into a 450 × 850 $km^2$

TABLE 3. Surface weather observations at Jackson, Wyoming. Period: 1045–1550 MST 21 July 1987. Ceiling in 100 m, S: scattered, B: broken, O: overcast, X: obscured, E: estimated, ff in m $s^{-1}$.

| MST | UTC | Clouds and ceiling | Weather | Temp (°C) | ddff |
|---|---|---|---|---|---|
| 1045 | 1745 | E9-B 30-O | R- | 12 | 0000 |
| 1146 | 1846 | 8-S 15-B 30-B | | 15 | 0000 |
| 1245 | 1945 | 12-B 24-B 37-O | | 16 | 0403 |
| 1300 | 2000 | 9-B 24-O | TRW- | | 0305 |
| 1310 | 2010 | 0.3-X RAIN | TRW HAIL | | 2818 |
| 1320 | 2020 | E9-O | TRW- | | 3008 |
| 1345 | 2045 | E9-B 24-O | TRW | 11 | 1606 |
| 1447 | 2147 | E12-B 24-O | TRW | 12 | 1605 |
| 1550 | 2250 | E12-B 24-O | RW | 11 | 1803 |

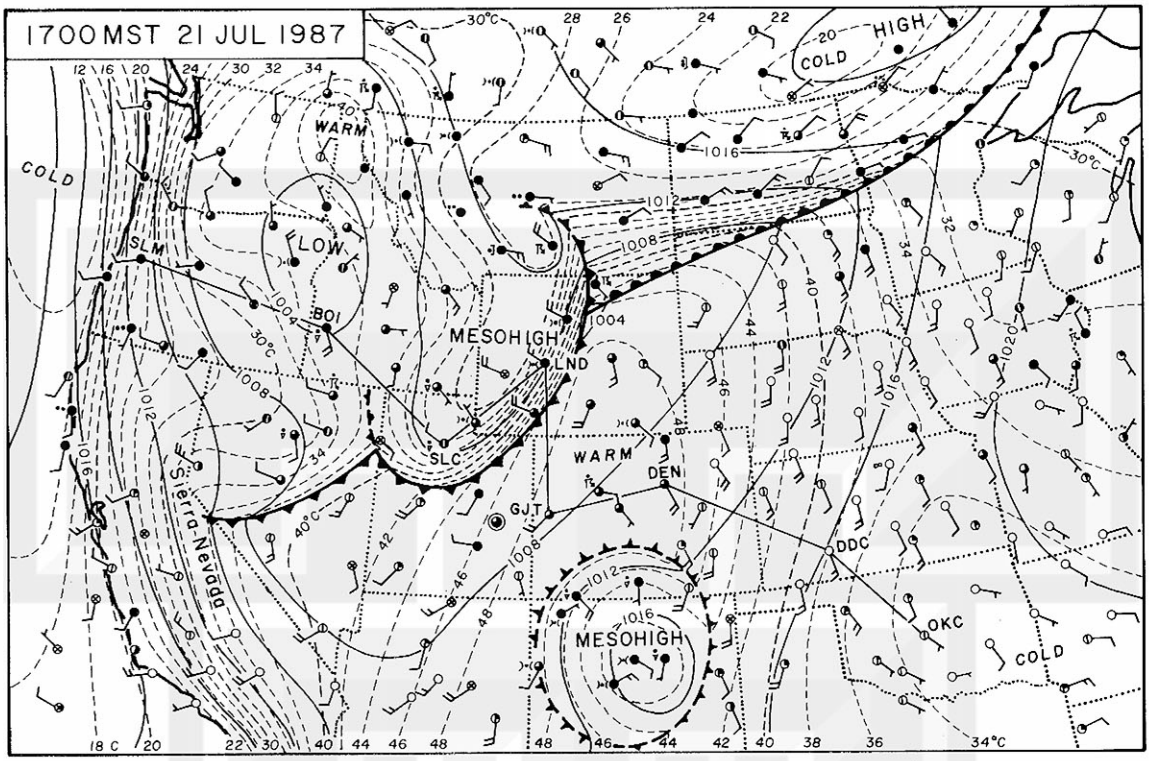


FIG. 18. A reanalysis of the NMC surface map at 1700 MST (00Z) with isotherms of potential temperatures in °C. The Teton–Yellowstone Tornado ended approximately 3 hours before this map time.

sized mesohigh at 1700 MST. Another mesohigh is seen over New Mexico. This map is a reanalysis of the NMC surface map at 00Z and isobars are drawn at 4-mb intervals. Because the elevation of some stations in the western regions exceeds 2000 m MSL, isotherms of potential temperature in °C were drawn instead of temperature isotherms. As expected, a 15°C cooling in potential temperature is seen inside the large mesohigh centered over western Wyoming. A line connecting OKC–DDC–DEN–GJT–LND–SLC–BOI–SLE was used later in producing vertical cross sections.

### *c. Mesoanalysis with altimeter setting*

Time plots of hourly and special observations depicted an early stage of a mesohigh in southern Idaho at 0900 MST. It expanded rapidly toward the northeast, passing the tornado area shortly before 1400 MST (see isochrones in Fig. 19).

In order to achieve a mesoanalysis over high terrain, we have to make use not only of the hourly but also special observations during weather events. Unfortunately, sea level pressure $P_0$ is reported only once every hour, necessitating an additional use of altimeter setting $A$ available from most airport stations at special observation times. However, altimeter setting and sea level pressure are basically different and their difference increases with station elevation when the air temperature is warmer or colder than the standard atmosphere.

Because 21 July was a hot summer day, altimeter settings were significantly higher than sea-level pressures at high elevation stations (see Fig. 20). At Laramie (LAR) for instance, the altimeter setting was 12 mb higher than the sea level pressure practically the whole day. If one tries to analyze pressure fields by mixing $P_0$ and $A$, the pressure pattern will turn into bubble highs and lows encircling reporting stations at high elevation.

In order to overcome this problem, the mean sea level pressure $\bar{P}_0$ at each station for the analysis period 0700–1800 MST (1400–0100 UTC) was computed first and plotted on the map, along with the mean vector wind at the station. Then the isobars of $\bar{P}_0$ were contoured for every millibar by using all available stations. Likewise, the mean altimeter setting $\bar{A}$ was computed at each available station for the same period, finding that $\bar{A}$ is 2 to 12 mb higher than $\bar{P}_0$.

Time sections in Fig. 21 were obtained by shifting the value of $\bar{A}$ downward until it coincides with $\bar{P}_0$. Hourly and special-observation pressures were connected with full lines when pressure traces were available. If not available, pressures were connected with dashed lines. The top diagram shows an incipient stage of the mesohigh, which gave rise to the pressure increase between 0900 and 1230 MST and the corresponding

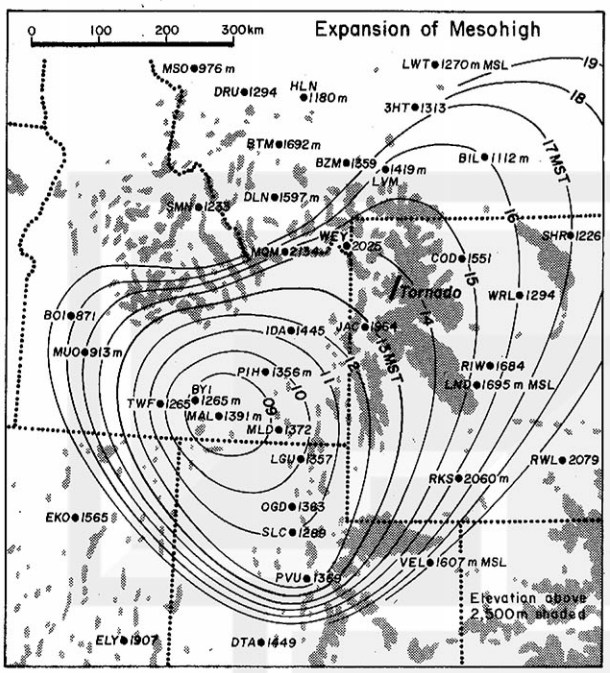


FIG. 19. Hourly isochrones of the mesohigh boundary on 21 July 1987. Areas of mountains above 2500 m are shaded.

outflow winds at Burley (BYI), Idaho. The same mesohigh affected Pocatello (PIH), Idaho 100 km to the northeast of BYI, causing a strong outflow centered at 1315 MST.

At Jackson Hole Airport, pressure began falling at 0800 MST, reaching a minimum at 1300 MST when the mesocyclone center was passing nearest to the station. Cody (COD), Wyoming was located to the north of the cold front where the wind direction before the mesohigh was from the northerly direction, and pressure rose over 4 mb during the passage of the mesohigh.

### *d. Mesoanalysis of the mesocyclone*

Although JAC was the only reporting station within the mesocyclone circulation, the mesoscale pressure field can be delineated by the mesoanalysis technique of time–space conversion devised by Fujita et al. (1956). First, the translational speed of the mesocyclone was estimated to be 25 m $s^{-1}$, based on winds aloft and the motion of the tornado cloud top determined from GOES East and West pictures. Second, the direction of the cloud motion was assumed from the 204° azimuth, the orientation of the tornado damage in Fig. 3.

Under the assumption that the mesocyclone moved at the constant rate of 25 m $s^{-1}$ from 204°, positions of the cloud at 10-min intervals are shown in the upper map of Fig. 22. The best estimate of the touchdown time was 1328 MST (2028 UTC) and the liftoff time, 1354 MST (2054 UTC). This map shows that the mesocyclone center passed 20 km east-southeast of JAC at 1300 MST (2000 UTC) when JAC reported the minimum pressure. The location of the straight-line wind damage at Teton Village is indicated by a short arrow from the 280° direction. The lower map presents the mesocyclone, mesohigh, and cold front discussed earlier. In analyzing the pressure field, pressure-trace tendencies at reporting stations were used as additional information for determining the pressure pattern from time sections.

It should be emphasized that the mesocyclone was located near the intersection of a warm front and a mesohigh boundary. The importance of severe storm formation at the intersection of arc clouds or mesohigh boundaries has been emphasized by Purdom (1986), and the process of this mesocyclone formation appears to be very similar to his conceptual model.

## 4. Infrared temperature of the parent tornado cloud

Because the Teton–Yellowstone tornado was spawned by a mesocyclone, infrared and visible pictures in Fig. 23 were presented in an attempt to show the parent cloud and its environment at 1404 MST (2104 UTC) scan time, approximately 10 min after the end

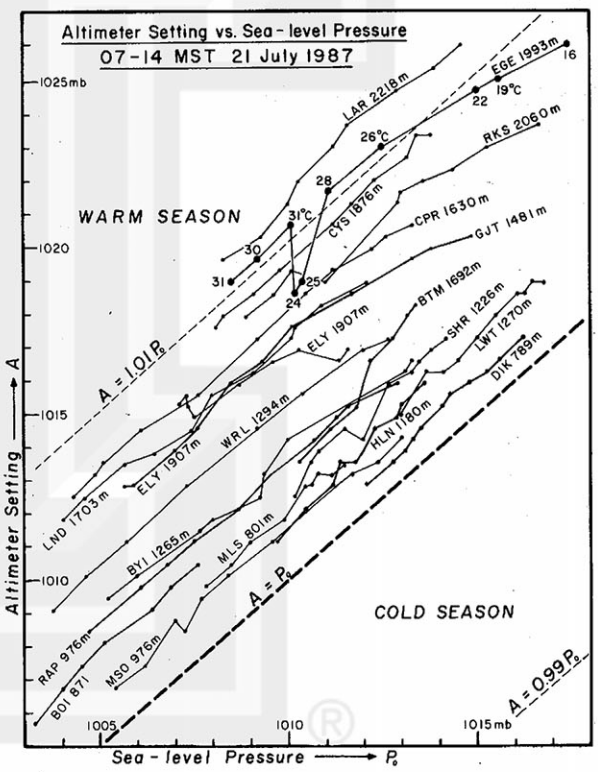


FIG. 20. Altimeter setting and sea-level pressure reported hourly from surface stations in the northwestern Rockies. Altimeter setting, computed from standard atmosphere, is higher than sea-level pressure in warm season because the latter decreases as temperature increases. At Eagle (EGE), Colorado, $A - P$ (altimeter setting minus sea-level pressure) decreased by 2 mb corresponding to a 4° to 7°C cooling. The decrease was attributed to the increase of $P$.

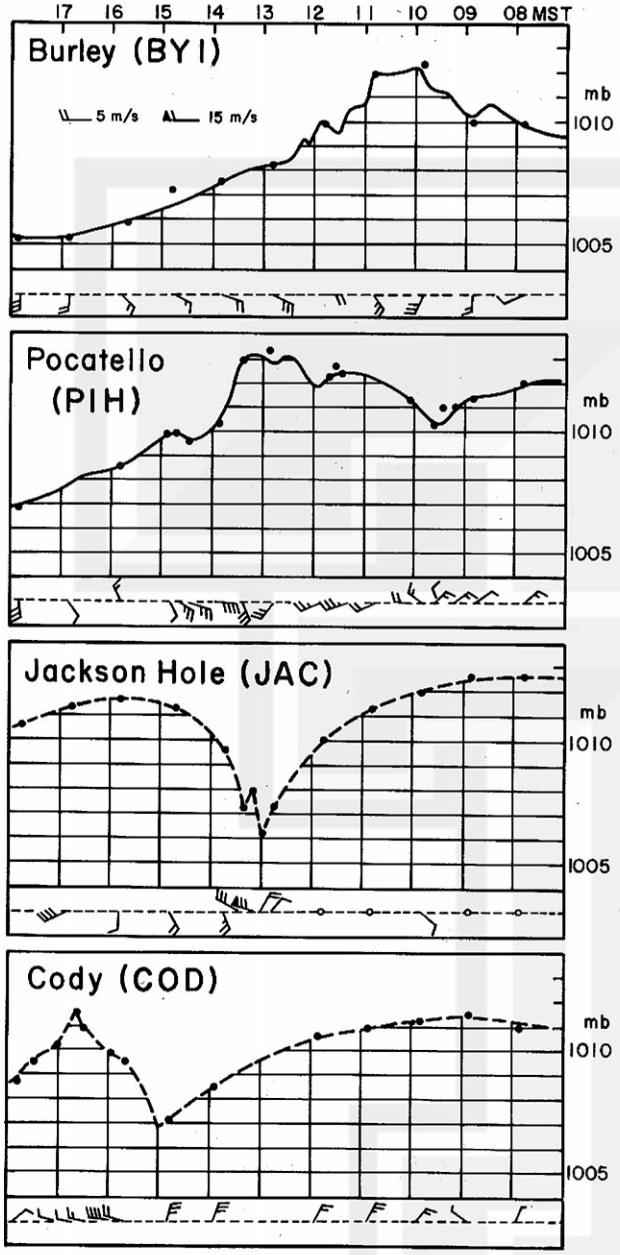


FIG. 21. Time sections at BYI, PIH, JAC, and COD, showing the expansion and advancement of the mesohigh. The center of the parent mesocyclone passed east-southeast of JAC at 1300 MST. For station locations, refer to Figs. 1 and 19.

of the tornado. It was found, however, that this type of infrared imagery is not capable of showing the mesocyclone cloud hidden inside a vast area of high-level cirrus clouds extending from Idaho to western Wyoming and Montana. Various techniques of infrared temperature mapping were explored for depicting complicated temperature patterns before, during, and after the tornado-bearing stage of the mesocyclone cloud top.

The visible picture depicts mountain waves behind high mountain ranges oriented perpendicular to the strong moisture flow from Utah and Colorado to Wyoming. These ranges are Unita Mountains (4124 m), Wind River Range (4208 m) west of LND, and Big Horn Mountains (4104 m). Numerous cloud streets over the high Rockies were disappearing along the

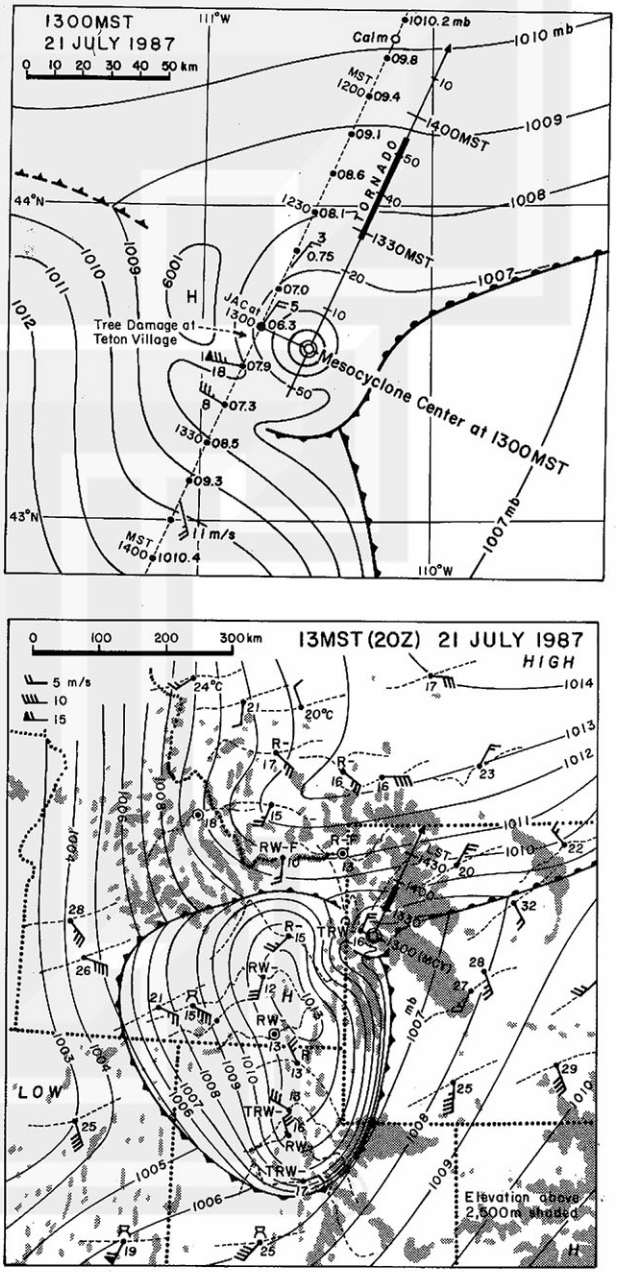


FIG. 22. Upper map: Isobars and path of the mesocyclone determined by combining the tornado damage, positions of cloud tops, and surface weather observations at JAC. Lower map: Mesoanalysis map at 1300 MST, showing the location of the Mesocyclone (MCY) in relation to cold front and mesohigh boundary. Dashed lines at stations denote pressure-tendency traces.

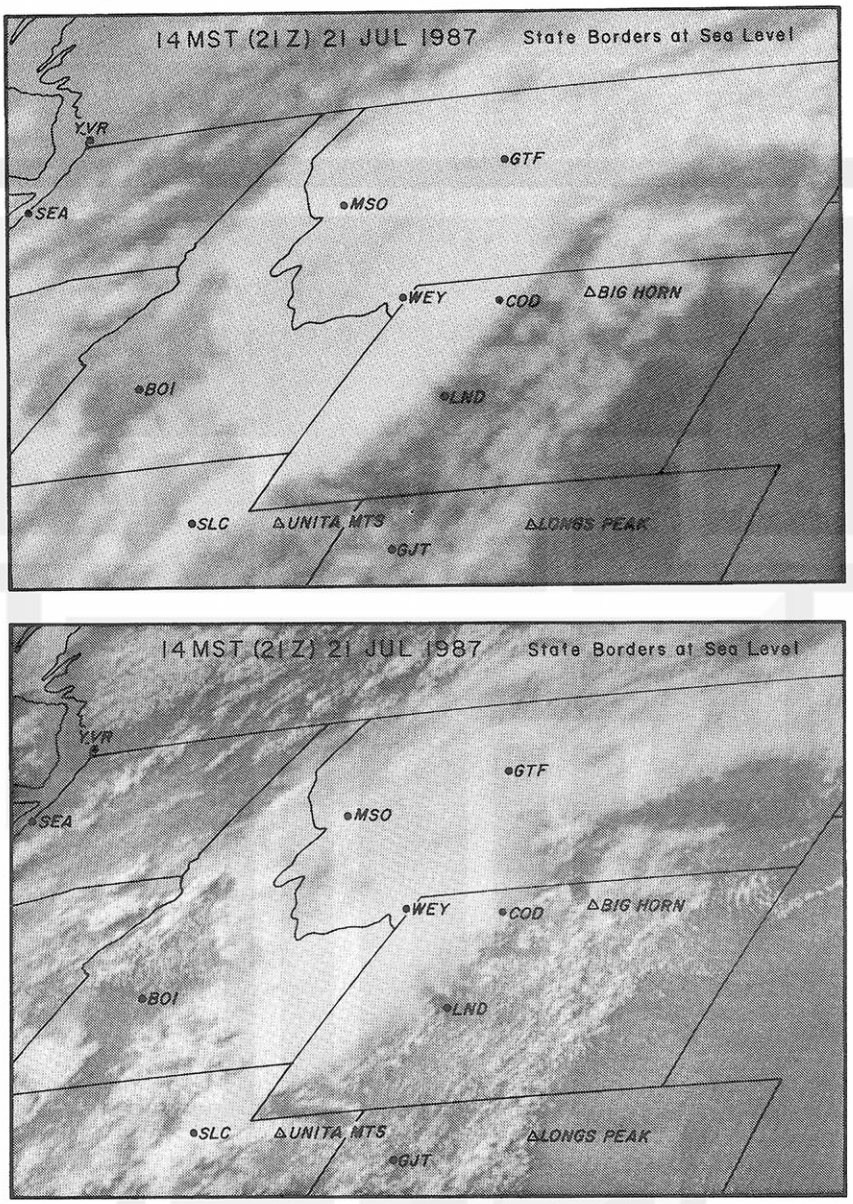


FIG. 23. Infrared (upper) and visible (lower) pictures at 1404 MST scan time, 10 min after the end of the tornado which was on the ground between 1328 and 1354 MST. State borders drawn are at sea level.

foothills. The northward flow toward the parent cloud converged orographically while passing over Green River Valley between Wind River Range and Salt River Range, north–south mountains on the Wyoming side of the Idaho border.

*a. Gridding at cloud-top level*

Operational GOES pictures include the grids which coincide with geographic features at sea level. As a result, objects at high elevations deviate toward the direction away from the subsatellite point on the equator. The amount of deviation increases in proportion to the MSL height.

Let $\delta$ be the geocentric angle between subsatellite point and cloud. It can be computed by a spherical trigonometric equation,

$$\cos\delta = \cos\phi \cos(\theta - \theta_0) \qquad (1)$$

where $\phi$ and $\theta$ are latitude and longitude of the cloud, respectively, and $\theta_0$, the subsatellite longitude. By using the data for the parent cloud at 1400 MST, $\phi = 44.3°$N, $\theta = 110.1°$W, and $\theta_0 = 74.7°$W, we have

$$\delta = \cos 0.583 = 54.3°. \quad (2)$$

The zenith angle, $\zeta$, of GOES East at the parent cloud is computed by solving an oblique plane triangle, including satellite, parent cloud, and earth's center. Thus we have

$$\zeta = 63.5°. \quad (3)$$

The satellite-viewed position of the cloud top will deviate from the sea level grid by

$$P = h \tan\zeta \quad (4)$$

where $P$ denotes the length of the deviation vector. For computation equations on the ellipsoidal earth, refer to Fujita (1982). Using the 13-km height of the parent cloud and the zenith angle in Eq. (3), we obtain

$$P = 13 \times 2.01 = 26 \text{ km}. \quad (5)$$

This means that sea level grids cannot be used in locating the parent cloud, because the error is 26 km (16 mi).

*b. Infrared isotherms on elevated grids*

In determining the accurate position of the parent cloud in the cloud-top temperature field, the state boundaries in Fig. 24 were gridded at 13-km MSL, the estimated height of the highest cloud identified by a small triangle encircled by a −63°C isotherm.

A new technique of 3-D isotherms was developed by using black and white isotherms on gray background. In selecting either black or white isotherms, it was assumed that the illumination light shines from the northwest on the topographic height proportional to the negative value of IR temperatures in °C. This means that the coldest temperature is identified as the highest point of the 3-D topography. In emphasizing small temperature variations inside anvil clouds, isotherms were drawn at 10°C intervals between +30° and −50°C, 2°C intervals between −50° and −60°C, and 1°C intervals below −60°C.

*c. Parent cloud of the Teton–Yellowstone Tornado*

An attempt was made to single out the temperature pattern of the overshooting top of the parent cloud


FIG. 24. A 3-D pattern of infrared temperature at 1404 MST scan time. State boundaries in this figure are gridded at 13 km MSL.

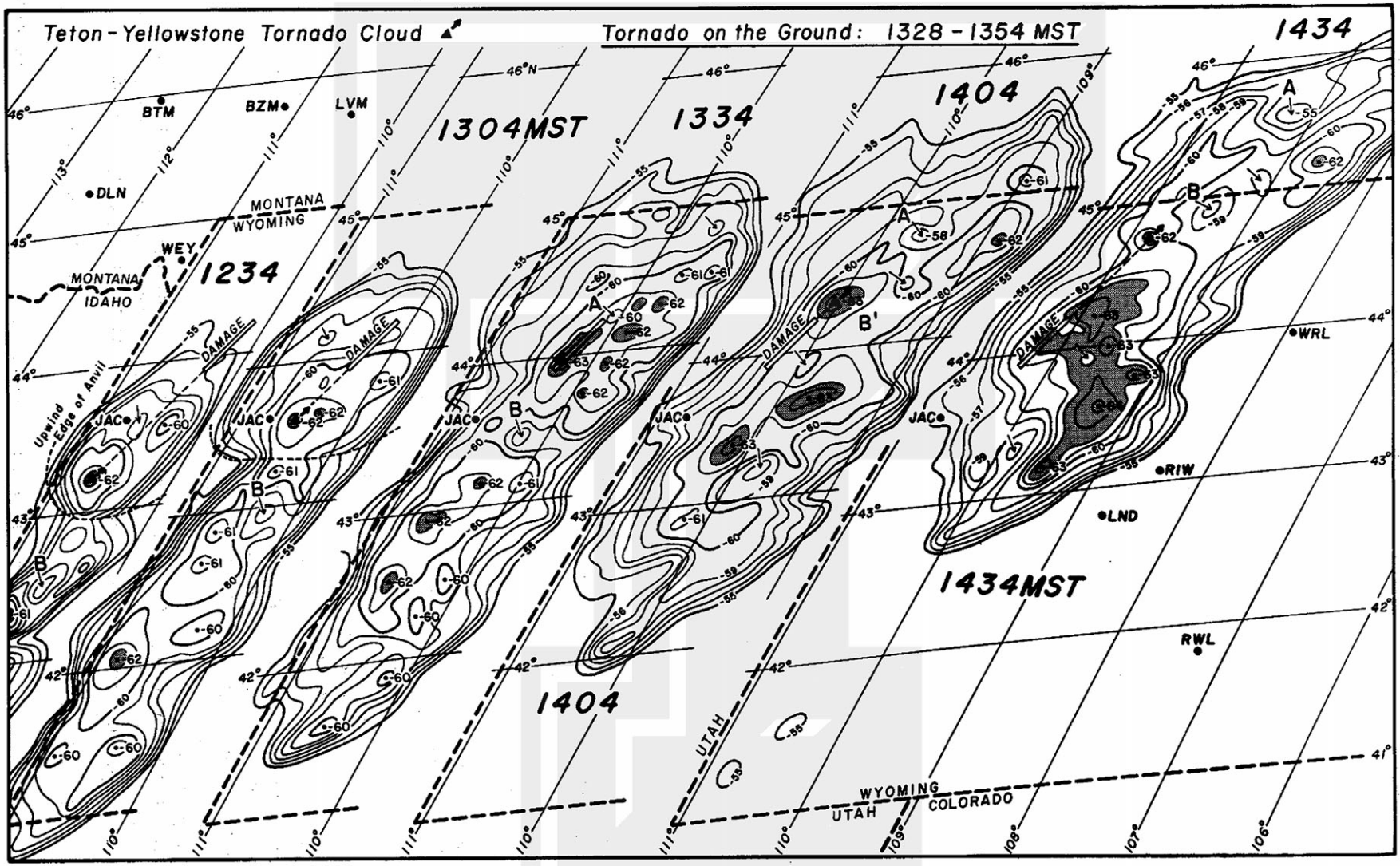


FIG. 25. Isotherms of anvil-top temperature fields, derived from GOES East infrared temperature. Two warm spots are identified by letters A and B. Geographic grid lines are computed at 13 km MSL on the ellipsoidal earth.

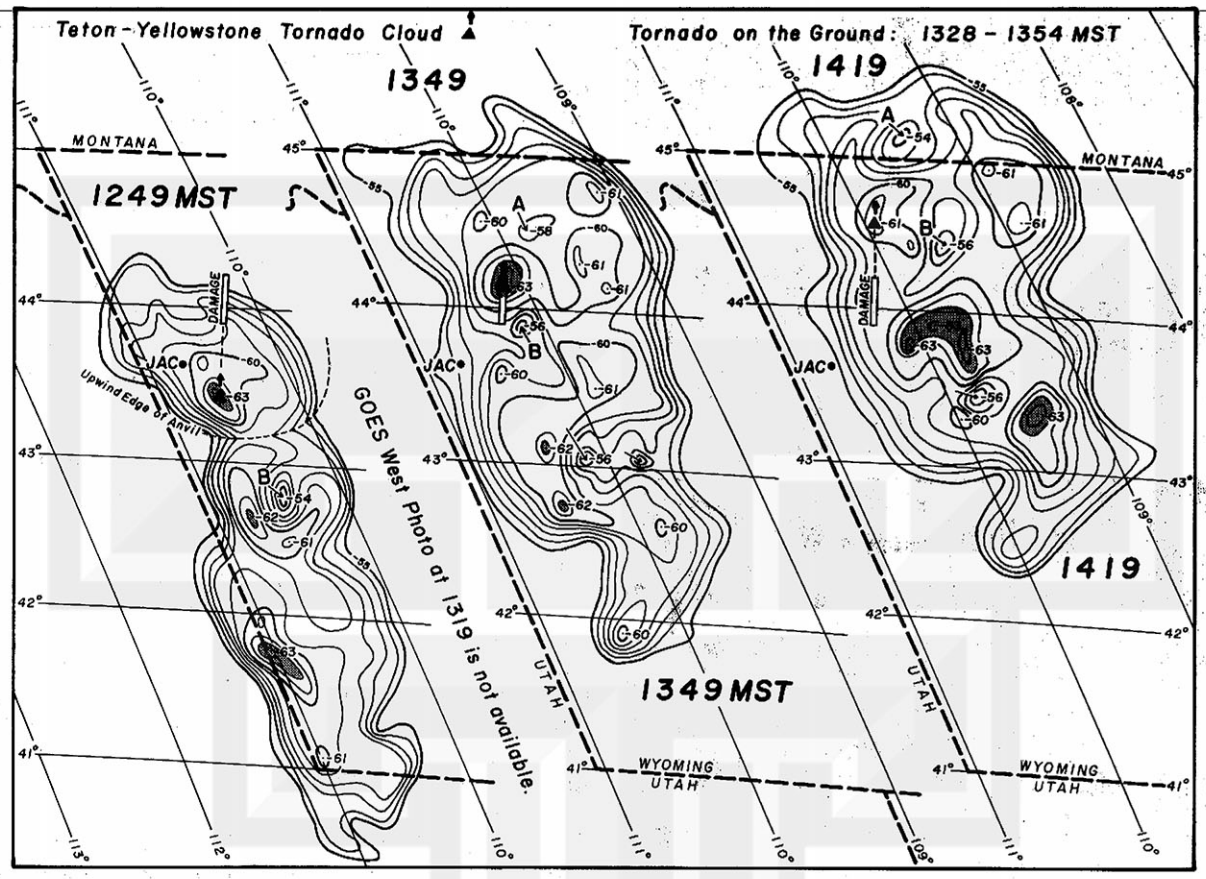


FIG. 26. Isotherms of the anvil-cloud complex derived from GOES West infrared temperature. Times indicated are scan time in MST. Geographic grid lines are computed at 13 km MSL on the ellipsoidal earth.

which left behind a 39-km long damage path. A total of eight pictures from GOES East and West were analyzed with 1°C contours. As shown in Figs. 25 and 26, a small but distinct cold cloud top moved directly over the damage area at 25 m $s^{-1}$. Assuming that the damage occurred beneath this cloud, the touchdown and liftoff times of the tornado were computed as 1328 MST and 1354 MST, respectively. The fast-moving tornado was on the ground for 26 min.

The first picture (IR temperature pattern) by GOES East at 1234 MST shows a growing anvil cloud with its upwind edge in the vicinity of 43°N latitude and 111°W longitude. A −62°C cloud top on the upwind side of the anvil was moving toward the damage area. At 1249 MST, 15 min after the first picture, GOES West depicted a −63°C cloud top and the upwind edge of the anvil cloud from a different perspective, looking from above the Pacific.

A −62°C cloud top was to the east of JAC at 1304 MST, 4 min after the station reported the lowest sea level pressure 1006.1 mb. The parent cloud at 1334 MST was over the worst damage area between Gravel Ridge and Enos Lake. The −63°C cloud in the GOES West picture at 1349 MST was near the end of the damage area and the tornado lifted off 5 min after this picture. At 1404 MST, 10 min after the end of the tornado, the cloud-top temperature was still cold, −63°C. As far as we know, no damage was found beneath this cold cloud. The GOES West picture at 1419 MST shows a −61°C top and GOES East picture at 1434 MST, a −62°C top, indicating warming of the parent cloud.

Table 4 summarizes the pixel counts of the parent cloud in eight GOES East and West pictures from digital data analyses. This result shows clearly that the

TABLE 4. Pixels of cloud-top temperatures above the Teton–Yellowstone Tornado cloud. Numbers in the table denote the cumulative counts of pixels with temperatures of −61, −62, −63, and −64°C or lower. MST denotes the scan time.

| MST | UTC | GOES | −61°C | −62°C | −63°C | −64°C | Remarks |
|---|---|---|---|---|---|---|---|
| 1234 | 1934 | East | 5 | 3 | — | — | |
| 1249 | 1949 | West | 8 | 4 | 2 | — | |
| 1304 | 2004 | East | 15 | 2 | — | — | |
| 1334 | 2034 | East | 24 | 8 | 2 | — | Tornado |
| 1349 | 2049 | West | 19 | 12 | 2 | — | Tornado |
| 1404 | 2104 | East | 27 | 11 | 1 | — | |
| 1419 | 2119 | West | 4 | — | — | — | |
| 1434 | 2134 | East | 6 | 2 | — | — | |

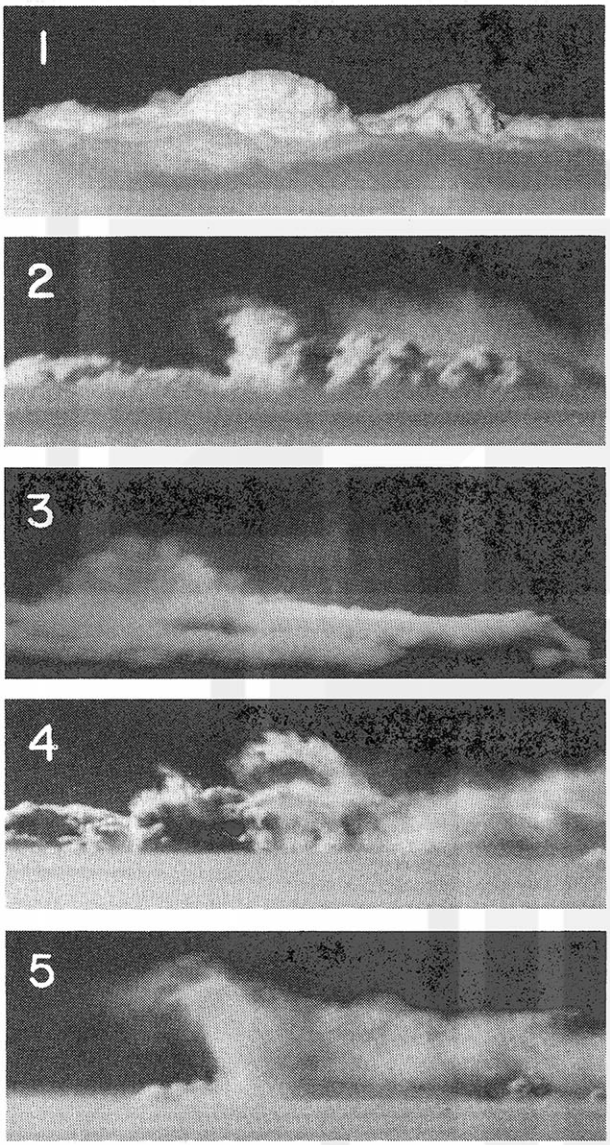


FIG. 27. Five types of anvil-top clouds photographed by the author from a Lear Jet at 12.5 km (41 000′) MSL over the Midwest. 1) Clean overshooting domes, 2) curly-hair cirrus, 3) fountain cirrus, 4) flair cirrus, and 5) geyser cirrus.

−61°C or colder pixels increased about 10 min before the tornado and decreased rapidly 10 min after the tornado, reaching a peak during the tornado. Although pixel counts are low, similar changes in pixel characteristics occurred at −62°C and −63°C temperatures.

### *d. Hypotheses and motion of the warm wake*

Another interesting phenomenon at the cloud-top height is the formation and movement of two enclosed warm areas A and B identified in Figs. 25 and 26. This phenomenon was first reported by Mills and Astling (1977) who introduced the term warm spot. They attributed the warming to high emissivity of the overshooting dome. In studying the infrared signature of downburst thunderstorms, Fujita (1978) found two types of warming areas, the one located on the upwind side of a bow echo at downburst stage and the other, downwind of an overshooting area.

For nowcasting and forecasting severe thunderstorms, McCann (1982) obtained a statistical evidence that V-shaped wakes are highly correlated to the occurrence of severe storms, strong tornadoes in particular. After examining numerous Lear Jet pictures of thunderstorm tops taken in the 1970s, Fujita (1982) postulated that cirrus clouds in the lowermost stratosphere above the anvil surface are the major contributors to the warming, calling the cloud the stratospheric cirrus. Shortly thereafter, Heymsfield et al. (1983) argued that they could not explain the magnitude of the warming based on the stratospheric cirrus, because the height and the coverage of the cirrus, obtained stereoscopically, was insufficient. Meanwhile, we are aware of the fact that small-sized fuzzy cirrus clouds cannot be used as reliable stereoscopic pairs for height computations.

Presented in Fig. 27 are semihorizontal views of the stratospheric clouds selected from the author's Lear Jet picture file. Their five types are 1) *clean overshooting domes* associated with little or no stratospheric cirrus; 2) *curly-hair cirrus,* originating at the head of an overshooting tower; 3) *fountain cirrus* which splashes up like a fountain, 1 to 2 min after an overshooting dome

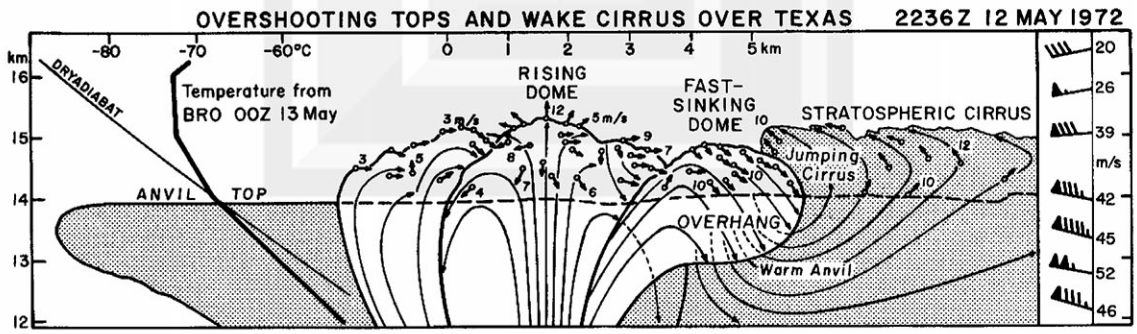


FIG. 28. Motion vectors of the cloud elements of overshooting domes and stratospheric cirrus atop a severe thunderstorm southeast of Laredo, Texas. Vectors were computed from six horizontal pictures at 1 sec intervals taken from the left window of a Lear Jet flying 92 km away from the cloud. This cloud became a right-deviating storm later, leaving behind a 72-km long path of F0 damage. One funnel cloud aloft was sighted over the damage area.

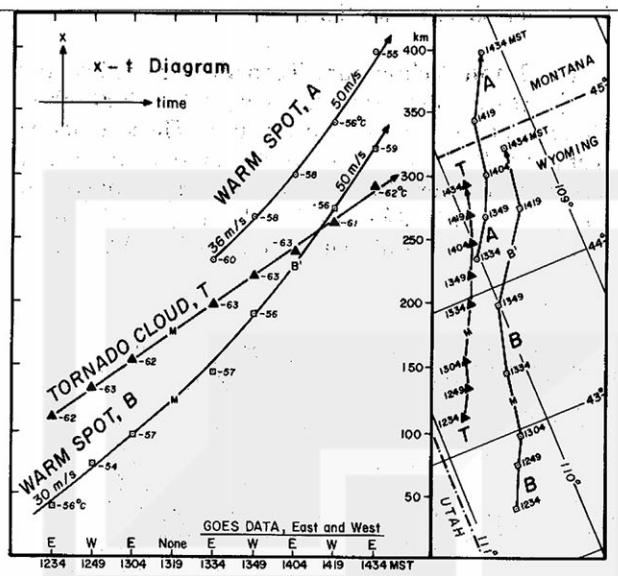


FIG. 29. Infrared temperature and movement of the tornado cloud T, and two warm spots A and B, tracked on the cloud-top isotherm maps in Figs. 25 and 26.

collapses into an anvil; 4) *flare cirrus* which jumps 1 to 3 km above the anvil surface and move upwind like a flare; 5) *geyser cirrus,* bursting up 3 to 4 km above the anvil surface like a geyser. The stratospheric cirrus drifting away from the region of the jumping cirrus, flare or geyser shaped, often extends several hundred kilometers, covering a very large area above an anvil surface.

In their recent paper, Adler and Mack (1986) reported that the temperature of overshooting tops is near adiabatic, and they proposed a model of the three classes of storm-top airflows. After running their one-dimensional model they concluded that no single hypothesis or model is able to explain the complicated nature of the warm wake and regarded the author's stratospheric cirrus as an alternate explanation. In an attempt to depict the motion field of anvil-top clouds, the author reanalyzed a sequence of telephoto pictures taken from a research Lear Jet. In contrast to the Adler–Mack model, the result in Fig. 28 shows a fast-sinking dome collapsing into the anvil surface without spreading into a large area. The jumping cirrus will drift away from an overshooting area if the above-anvil winds are faster than the translational speed of the overshooting area. If not, the jumping cirrus moves back toward the overshooting area which will be covered with a thin or thick veil of stratospheric cirrus.

The source of energy for generating the jumping cirrus has not yet been identified positively. However, the following three sources are the possible candidates: 1) Kinetic energy—kinetic energy of a collapsing dome while leaning downwind with an overhang shape will give rise to a splashing motion of the anvil-top airflow. 2) Potential energy—the downward displacement of the anvil beneath a collapsing overhang will warm the depressed anvil adiabatically, generating the buoyancy-originated potential energy. 3) Latent heat of fusion—photographic evidence that a clean dome turns into a fuzzy, glaciation-like appearance within a matter of one minute suggests the existence of the remnant supercooled water droplets inside an overshooting dome after its temperature falls below −40°C. The droplets near the overhang base will freeze upon contacting and mixing with frozen anvil particles. The latent heat of fusion, thus released, will result in an additional warming at the source of the jumping cirrus.

In light of the foregoing anvil-top characteristics, we shall examine the cloud-top temperature fields again. Seen in Figs. 25 and 26 are two warm spots A and B identifiable in successive temperature maps. Translational motions of these spots computed from Fig. 29 increased from 30 to 50 m $s^{-1}$ as these spots moved away from the source regions. On the other hand, the tornado cloud top moved at a steady rate of 25 m $s^{-1}$. A schematic cross section of the parent cloud in Fig. 30 shows the tropopause at 12.1 km and the overshooting top with a −63°C temperature at 13.1-km MSL. Anvil-top winds up to 13.5 km were approximately 47 m $s^{-1}$, which are rather strong for a sum-

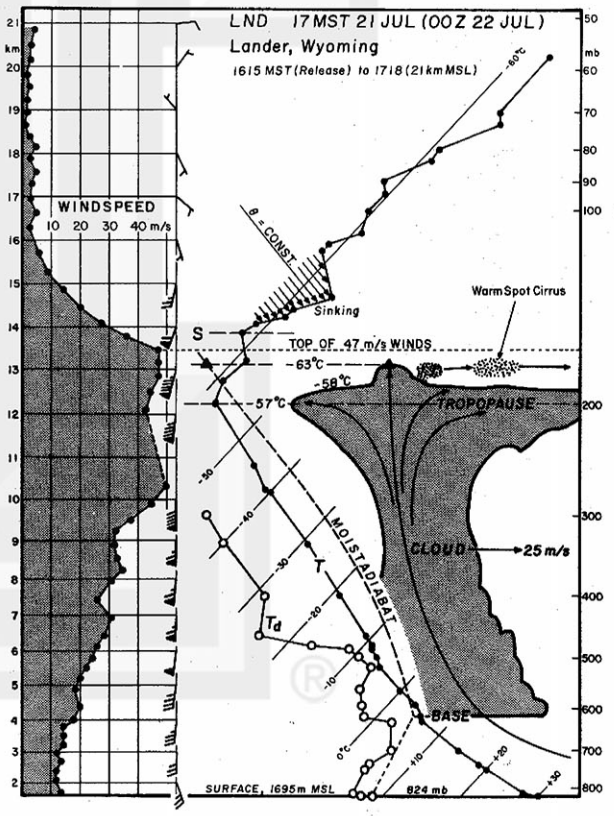


FIG. 30. A schematic cross section of the parent cloud. The lowest pixel temperature, −63°C, corresponds to the moist-adiabatic temperature at 13.1 km MSL. Note that the strong wind above the anvil extended to 13.5 km MSL, suggesting that the wind could transport the stratospheric cirrus above the anvil cloud at 50 m $s^{-1}$.

mertime thunderstorm. On the basis of these data, we may speculate that the warm spot caused by jumping-cirrus activity began drifting away at 30 m $s^{-1}$, slightly faster than the overshooting top. Then the speed increased to 50 m $s^{-1}$, the speed of the steering wind of the cirrus. Because of relatively low emissivity of stratospheric cirrus, the temperature of a warm spot decreases while passing over a cold anvil background and increases over a warm background.

## 5. Upper-air cross sections

The Teton–Yellowstone Tornado occurred beneath the jet stream that was associated with a 200-mb cyclone centered over the Oregon coast. The jet extended from over San Francisco, California to southern Canada, passing over SLC and GTF where the maximum wind speed at 11.8-km MSL (212 mb) was 57 m $s^{-1}$. The 100 and 200-mb winds at 17 MST (00Z) super-

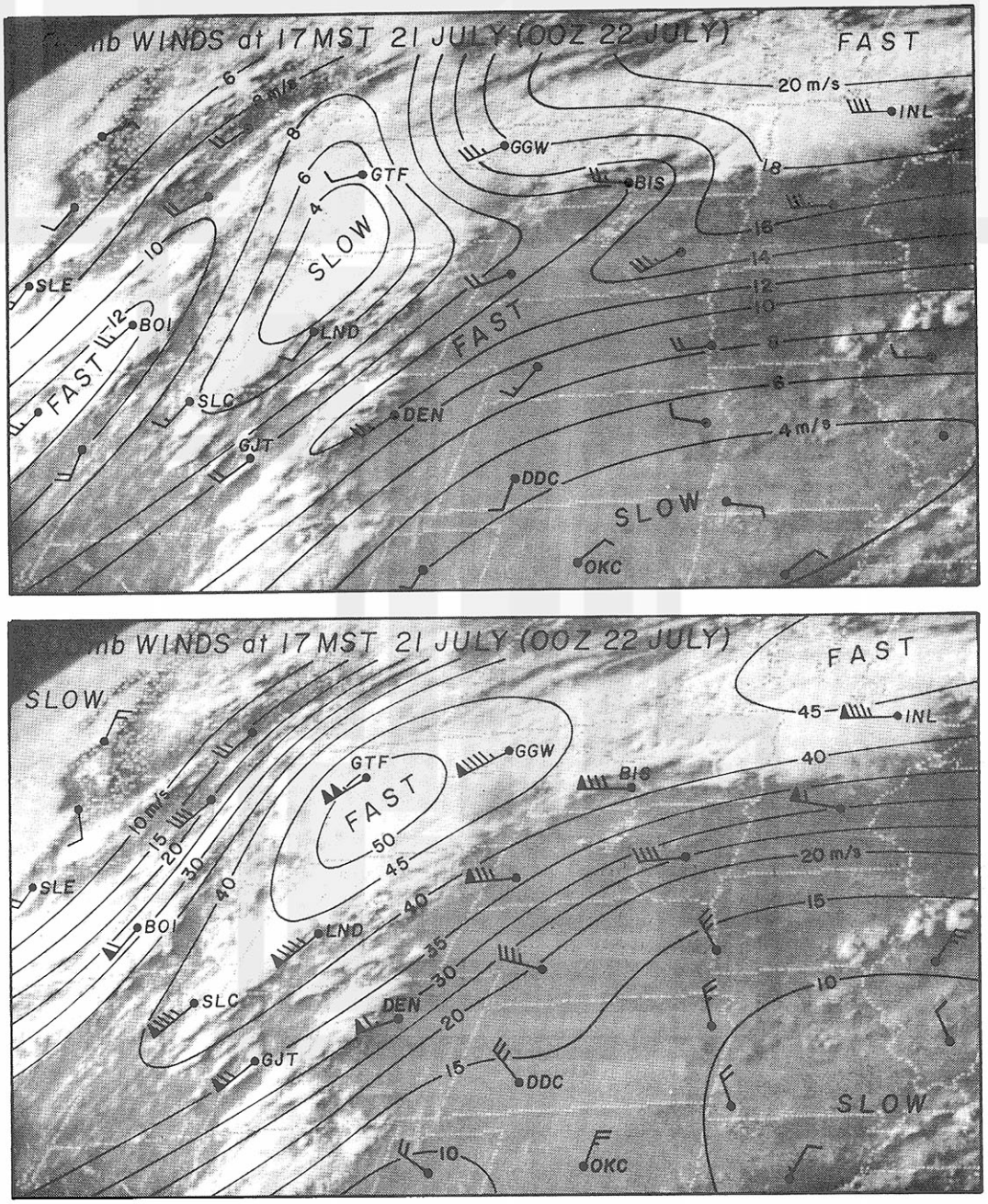


FIG. 31. Jet-stream winds at 20 mb and slow winds at 100 mb at 1700 MST (0000 UTC) superimposed upon the GOES East pictures starting at 1630 MST (2330 UTC). A slow-wind area at 100 mb (upper picture) is located directly above the high-wind core.

imposed upon the visible picture at 1630 MST show strong jet-stream winds at 200 mb. At 100 mb however, the wind speed dropped to less than 4 m $s^{-1}$ directly over the area of the high winds at 200 mb (see Fig. 31).

The phenomenon is seen more explicitly in the upper-air cross section in Fig. 32 made along the line connecting SLM–BOI–SLC–LND–GJT–DEN–DDC–OKC (refer to Fig. 18). Two dashed vertical lines at LND and SLC show the heights of missing winds aloft due to difficulties in tracking balloons. At LND, the elevation angle of the balloon at line S, approximately 1 km above the jet core, was 11.4° which is high enough for wind determinations. After reaching above line S, elevation angles increased gradually to 13.6°, indicating that the slow winds above the jet core are reliable and accurate. Another aspect of the winds aloft between 13 and 20 km MSL is a very systematic and gradual change in wind vectors in both vertical and horizontal directions. This evidence also increases the credibility of the measured winds.

Isotachs drawn in Fig. 32 show the height of the minimum winds (HMW) where the circumpolar easterlies at high altitudes change into southerlies or westerlies at low altitudes. The HMW over OKC at 110-mb height increases to 70-mb height over DEN and 60-mb height over SLC. However, it dips down slightly over the low-wind core.

A vertical cross section of temperature in Fig. 33 shows the large-scale tropopause at 14- to 15-km MSL on the equatorial side of the jet core and at 11- to 12-km MSL on the other side. A schematic view of the Teton–Yellowstone cloud extending to 13 km MSL is shown by a rectangular, tall box with horizontal lines of moist-adiabat isotherms. The cloud-top temperature, −63°C at the tornado time, was 8°C colder than the environmental temperature estimated from GJT, LND, and SLC soundings.

It is likely that the warming above the concave line S was caused by a mesoscale subsidence of stratospheric air descending toward the cold anvil cloud with a number of embedded overshooting domes. Although

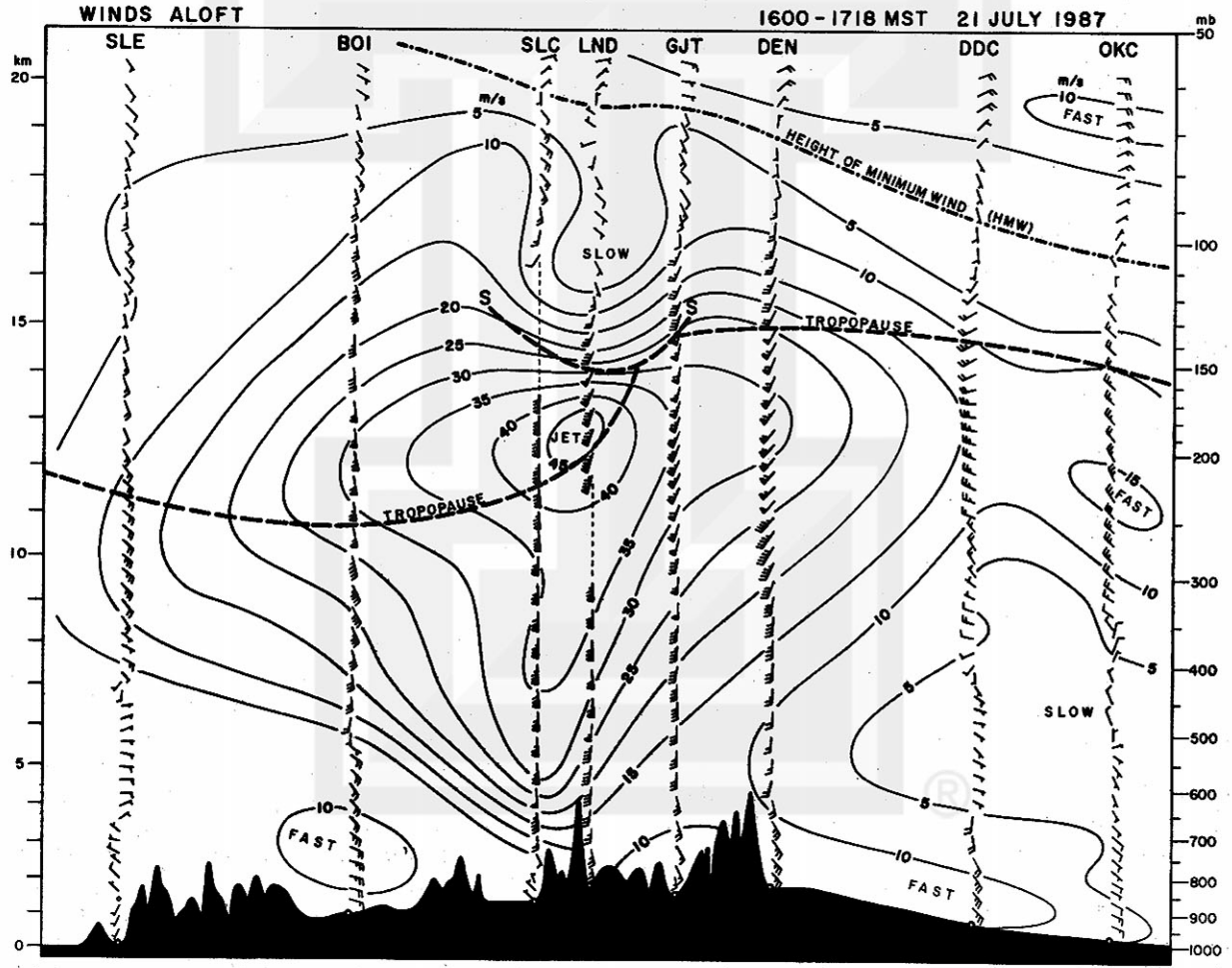


FIG. 32. A vertical cross section of winds aloft at 1700 MST 21 July 1987 (00Z 22 July 1987). The high-wind core above LND is topped by a low-wind core. Dashed line S denotes the base of the low-wind core. Note that the height of the minimum wind (HMW), extending from above OKC to BOI, dips slightly at the location of the low-wind core.

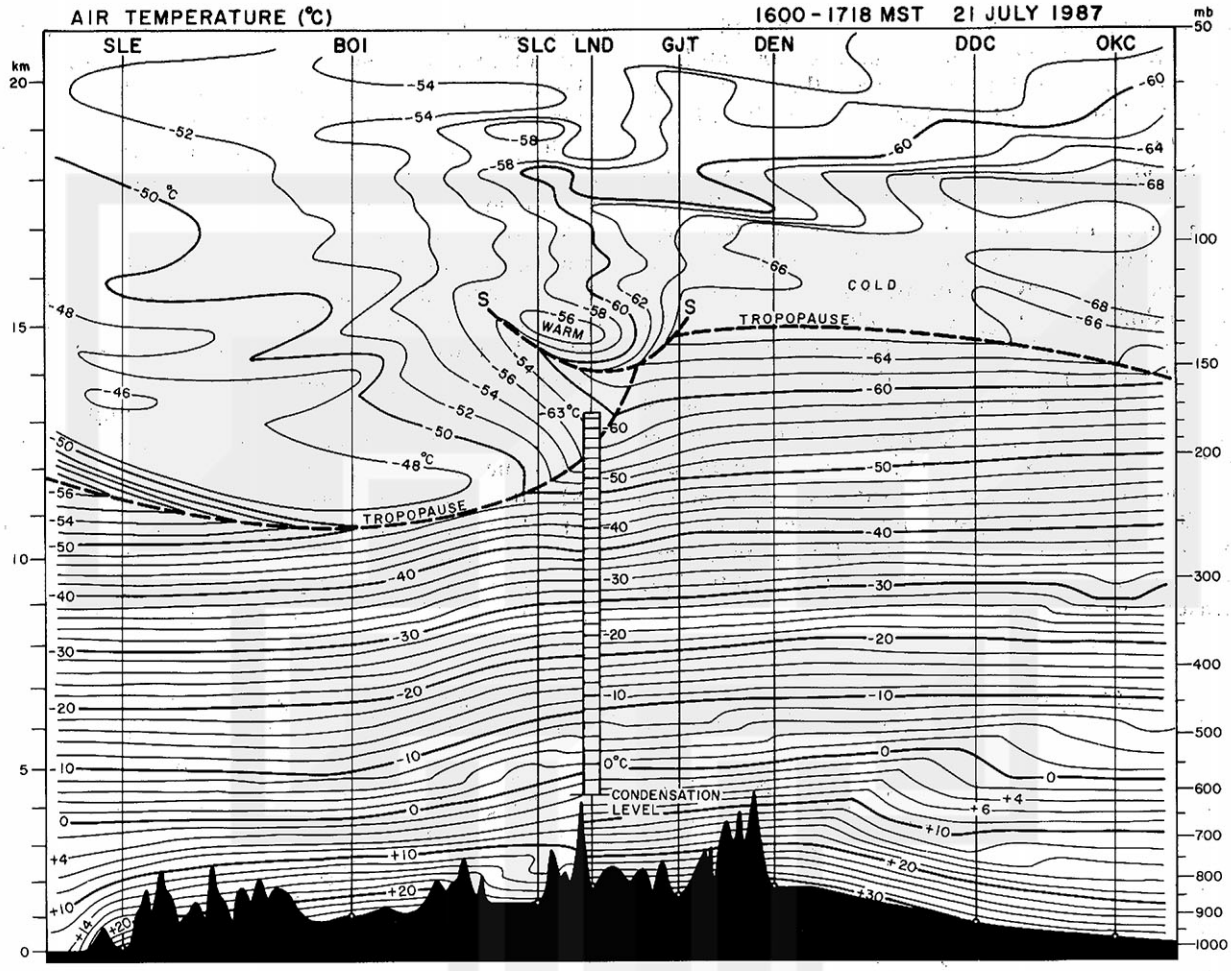


FIG. 33. A vertical cross section of temperature at 1700 MST. Schematic view of the parent cloud is shown by a tall, vertical column with the horizontal lines of moist-adiabat temperatures inside. The warm area above line S is likely to be caused by a mesoscale sinking motion.

an empirical evidence of a descending current at the lowermost stratosphere is hard to obtain, Fritsch and Maddox (1981) applied a fine-mesh, 20-level, equation model to the Mesoscale Convective Complex (MCC), obtaining a 5 to 10 cm $s^{-1}$ descending current, 1 to 2 km above an MCC top at 16 km MSL. On the basis of this numerical experiment and the evidence presented in Figs. 32 and 33, the author thinks that the mesoscale subsidence above the Teton–Yellowstone storm cloud is realistic.

A vertical cross section of potential temperature in Fig. 34 will provide us with another way of identifying a large-scale sinking on the polar side of the jet and a mesoscale sinking above the storm cloud. A combined examination of these three cross sections gives a definite impression that the suspected mesoscale sinking could cause the warm low-wind core topped by a depressed height of the minimum wind (HMW). It should also be noted that the cloud-top subsidence will increase the temperature of the anvil-top cirrus as it jumps up and mixes with the stratospheric air warmer than the free atmosphere outside the anvil area.

## 6. Summary and conclusions

The purpose of this research is to document the rare event of the Teton–Yellowstone tornado which left behind a wide-path damage swath, including a devastating tree damage rated F4. Identified in the damage area are four swirl marks of spinup vortices and 72 microburst outflows. The duration of the tornado estimated from the translational motion of the parent cloud top and the 39.2-km path length is approximately 26 min. In documenting the damage in the remote wilderness, the entire damage area was flown twice by Cessna aircraft and once by a photographic aircraft that took stereo-pair pictures, recording literally every single tree in the forest. Unexpectedly, most of the damage area was burned down by forest fires during the 1988 drought. Consequently, we are not able to perform fol-

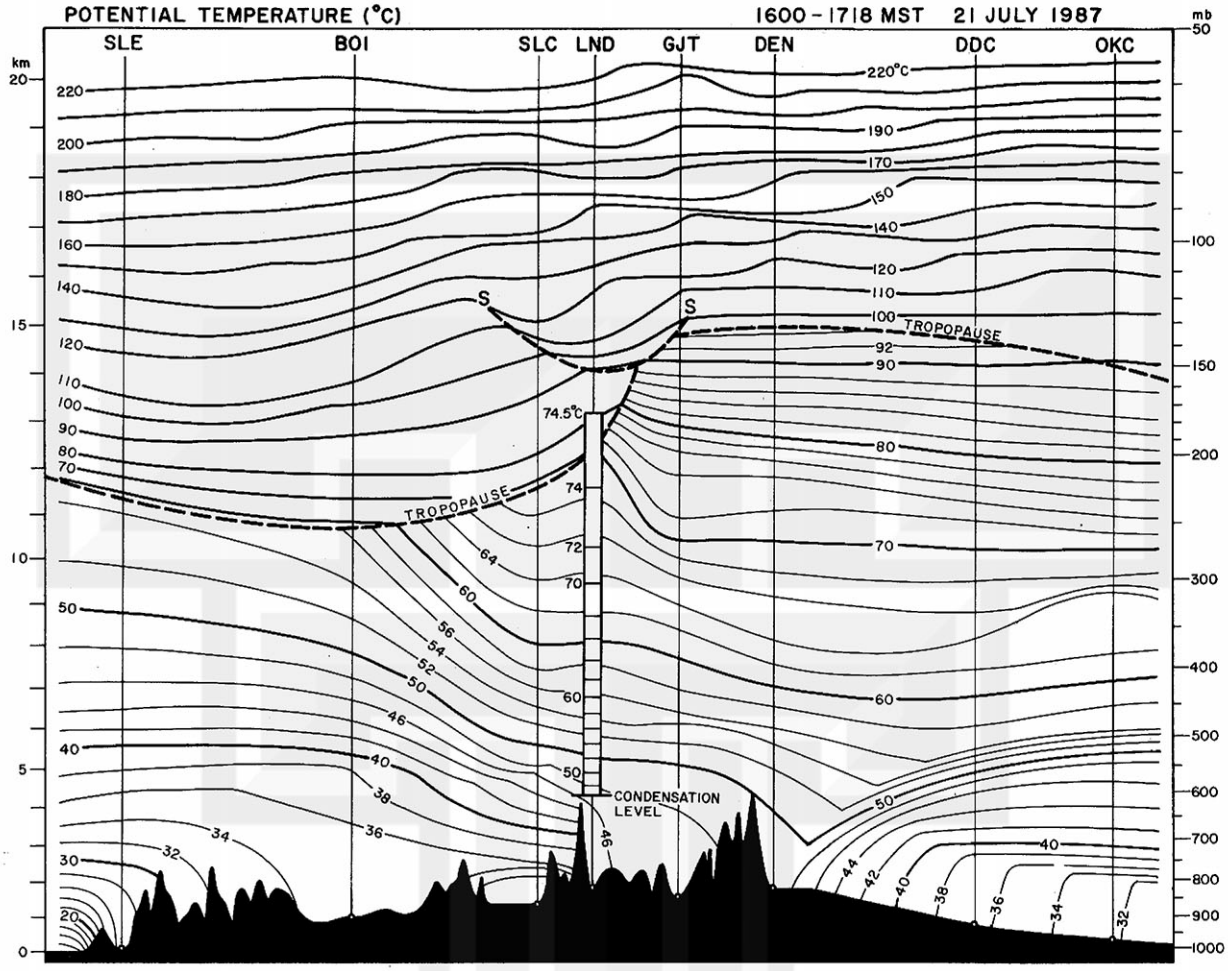


FIG. 34. A vertical cross section of potential temperature in °C. Severe-storms activity occurred between the prefrontal high tropopause and the postfrontal low tropopause. Line S denotes the base of the mesoscale sinking motion shown in Figs. 32 and 33.

low-up aerial photography and site visits for ecological studies.

A detailed mapping of GOES East and West data revealed that a cold-pixel cloud traveled over the damage area at 25 m $s^{-1}$. Found also are two warm spots enclosed inside the cold anvil area. On the basis of their thermal characteristics and movement, an attempt was made to explain these warm spots as being the stratospheric cirrus above the anvil cloud. It is recommended that satellite data, imagery and digital forms, are analyzed with the highest possible resolution along with other supporting data such as aerial stereophotos, radar, and synoptic data. An accumulation of such analyses will improve the method of nowcasting strong tornadoes in the western United States.

*Acknowledgments.* The author is grateful to the U.S. Forest Service of Teton Wilderness for providing important storm information and in assisting the site visits by Messrs. Brian E. Smith, James W. Partacz, and Bradley S. Churchill, staff members of the Wind Research Laboratory, The University of Chicago. After his low-altitude aerial photography, Mr. Brian Smith performed a painstaking identification of his pictures in completing the four local damage maps. As part of satellite data analysis, Mr. Jaime J. Tecson generated grid-point maps of GOES East and West cloud-top temperature.

This research has been sponsored by the National Science Foundation under Grant ATM85-16705, the National Oceanic and Atmospheric Administration/NESDIS under Grant NA85-AADRA064, and the National Aeronautics and Space Administration under Grant NGR 14-001-008.

## REFERENCES

Adler, R. F., and R. A. Mack, 1986: Thunderstorm cloud top dynamics as inferred from satellite observations and a cloud top parcel model. *J. Atmos. Sci.*, **43**, 1945–1960.

Agee, E., C. Church, C. Morris and J. Snow, 1975: Some synoptic aspects and dynamic features of vortices associated with the tornado outbreak of 3 April 1974. *Mon. Wea. Rev.*, **103**, 318–333.

Brandes, E. A., 1981: Finestructure of the Del City–Edmond tornadic mesocirculation. *Mon. Wea. Rev.*, **109**, 635–647.

——, 1984; Vertical vorticity generation and mesocyclone sustenance in tornadic thunderstorms: The observational evidence. *Mon. Wea. Rev.*, **112,** 2253–2269.

Brooks, E. M., 1949: The tornado cyclone. *Weatherwise,* **2,** 32–33.

Brown, R. A., W. C. Baumgarner, K. C. Crawford and D. Sirmans, 1971: Preliminary Doppler velocity measurements in a developing radar hook echo. *Bull. Amer. Meteor. Soc.,* **52,** 1186–1188.

Flora, S. D., 1954: *Tornadoes of the United States.* University of Oklahoma Press, 221 pp.

Fritsch, J. M., and R. A. Maddox, 1981: Convectively driven mesoscale weather systems aloft. Part II. Numerical simulations. *J. Appl. Meteor.,* **20,** 22–26.

Fujita, T. T., 1971: Proposed mechanism of suction spots accompanied by tornadoes. Preprints, *Seventh Conference on Severe Local Storms,* Kansas City, Amer. Meteor. Soc., 208–213.

——, 1978: Manual of downburst identification for Project NIMROD. SMRP Res. Pap. No. 156, The University of Chicago, 104 pp. [NTIS PB-286048.]

——, 1981: Tornadoes and downbursts in the context of generalized planetary scales. *J. Atmos. Sci.,* **38,** 1511–1534.

——, 1982: Principle of stereoscopic height computations and their applications to stratospheric cirrus over severe thunderstorms. *J. Meteor. Soc. Japan,* **60,** 355–368.

——, H. Newstein and M. Tepper, 1956: Mesoanalysis, an important scale in the analysis of weather data. U.S. Weather Bureau, Res. Pap. No. 39, U.S. Govt. Printing Office, Washington, DC, 83 pp.

Heymsfield, G. M., R. H. Blackmer, Jr. and S. Schotz, 1983: Upper-level structure of Oklahoma tornadic storms on 2 May 1979. I: Radar and satellite observations. *J. Atmos. Sci.,* **40,** 1740–1755.

Lemon, L. R., D. W. Burgess and R. A. Brown, 1978: Tornadic storm airflow and morphology derived from single-Doppler radar measurements. *Mon. Wea. Rev.,* **106,** 48–61.

McCann, D. W., 1983: The enhanced—V: A satellite observable severe storm signature. *Mon. Wea. Rev.,* **111,** 887–894.

Mills, P. B., and E. G. Astling, 1977: Detection of tropopause penetrations by intense convection with GOES enhanced infrared imagery. Preprints, *Tenth Conference on Severe Local Storms,* Omaha, Amer. Meteor. Soc., 61–64.

Purdom, J. F. W., 1986: Satellite contributions to convective scale weather analysis and forecasting. Preprints, *11th Conference on Weather Forecasting and Analysis,* Kansas City, Amer. Meteor. Soc., 295–314.

Root, C. J., and W. E. Barron, 1925: The Tri-state tornado of March 18, 1925. Climatological Data, Illinois Section, U.S. Weather Bureau, 12a–12d.

STORM DATA, 1984; Tornado outbreak in the Carolinas on 28 March 1984. National Climatic Data Center, Asheville, NC, Storm Data, 26, 45 pp.

——, 1987: Outstanding storms of the month, Monthly tornado maps. National Climatic Data Center, Asheville, NC, Storm Data, 29, Nos. 1–12.

Reprinted from MONTHLY WEATHER REVIEW, Vol. 117, No. 9, September 1989
American Meteorological Society